

Earth and Space Science



RESEARCH ARTICLE

10.1029/2021EA001675

Key Points:

- Automated geophysical instrument quality control based on a database of power spectral density (PSD) estimates
- Strict quality criteria on PSD estimates to verify the performance of geophysical instruments
- Operational for the Netherlands Seismic-Acoustic Network (NSAN) and extendable to other geophysical monitoring infrastructures

Supporting Information:

Supporting Information may be found in the online version of this article.

Correspondence to:

M. R. Koymans,
mathijs.koymans@knmi.nl




Citation:

Koymans, M. R., Domingo Ballesta, J., Ruigrok, E., Sleeman, R., Trani, L., & Evers, L. G. (2021). Performance assessment of geophysical instrumentation through the automated analysis of power spectral density estimates. *Earth and Space Science*, 8, e2021EA001675. <https://doi.org/10.1029/2021EA001675>

Received 22 JAN 2021

Accepted 19 JUL 2021

Performance Assessment of Geophysical Instrumentation Through the Automated Analysis of Power Spectral Density Estimates

M. R. Koymans¹ , J. Domingo Ballesta¹, E. Ruigrok¹, R. Sleeman¹, L. Trani¹ , and L. G. Evers¹ 

¹R&D Seismology and Acoustics, Royal Netherlands Meteorological Institute, De Bilt, The Netherlands

Abstract This study describes an automated data quality verification procedure supported by a database of power spectral densities (PSD) estimates for geophysical waveform data. The Royal Netherlands Meteorological Institute (KNMI) manages a 100-TB archive of continuous geophysical data collected from accelerometers, geophones, broadband seismometers, and infrasonic arrays deployed across the continental and Caribbean Netherlands. This rapidly expanding network at a scale of over 700 instruments makes the manual evaluation of data quality impractical and must be supported by data policies and automated methods. A technique is presented to compress and store PSD estimates in a database with a storage footprint of less than 0.05% of the raw data archive. Every week, the instrument performance is validated by comparing statistical properties of its latest monthly probabilistic PSD distribution to strict quality metrics. The criteria include thresholds based on global noise models, datalogger quantization noise models, constraints imposed by ambient noise conditions, and confidence intervals based on PSD estimates calculated from validated archived data. When a threshold is crossed, the station operator is alerted of the suspected degraded instrument performance, severely limiting the required amount of manual labor and associated human errors. The automated PSD assessment technique is applicable to accelerometers, geophones, broadband seismometers, infrasonic stations, and is demonstrated to be extendable to hydrophones, gravimeters, tiltmeters, and Global Navigation Satellite System receivers. The approach is therefore suitable for other geophysical monitoring infrastructures, for example, observational networks dedicated to continuous volcano monitoring. It is shown that it is possible to detect degraded instrument performance that may otherwise remain undetected.

1. Introduction

Geophysical monitoring infrastructures passively observe the effects of natural phenomena that continuously take place and evolve in the atmosphere, oceans, and the solid earth. At our disposal is a set of unique and complementary instruments and sensing techniques that each provide a piece of key insight toward understanding these processes. The different strengths and sensitivities of each different geophysical sensor and measurement contributes its part in a larger observational network. Because of this wide variety of sensors and data types, it is beneficial to find one universal data quality assessment technique that is effective for all instruments leveraged in a geophysical operational network.

The Royal Netherlands Meteorological Institute (KNMI) operates different types of geophysical instruments that are deployed in the Netherlands Seismic-Acoustic Network (NSAN), both in the continental Netherlands (KNMI, 1993) and Caribbean Netherlands (KNMI, 2006). The observational network (Figure 1) comprises over 700 instruments including geophones, accelerometers, broadband seismometers, infrasonic arrays, and four Global Navigation Satellite System (GNSS) receivers. The monitoring capability of the network is promptly expanded when new observations are required, or new sensing techniques become more affordable and accessible.

Most geophysical monitoring infrastructures are designed for the assessment of hazards that include, for example, natural and induced earthquakes (Camelbeeck & van Eck, 1994; Spetzler & Dost, 2017), explosions (Ruigrok et al., 2019), infrasonic events (Evers et al., 2007), observations of volcanic unrest (Carbone & Greco, 2007; Sparks et al., 2012), and to verify compliance with the Comprehensive Nuclear-Test-Ban Treaty (Coynne et al., 2012), followed by rapid dissemination of information to the public. With advances in sensing

© 2021. The Authors.

This is an open access article under the terms of the [Creative Commons Attribution-NonCommercial License](https://creativecommons.org/licenses/by-nc/4.0/), which permits use, distribution and reproduction in any medium, provided the original work is properly cited and is not used for commercial purposes.

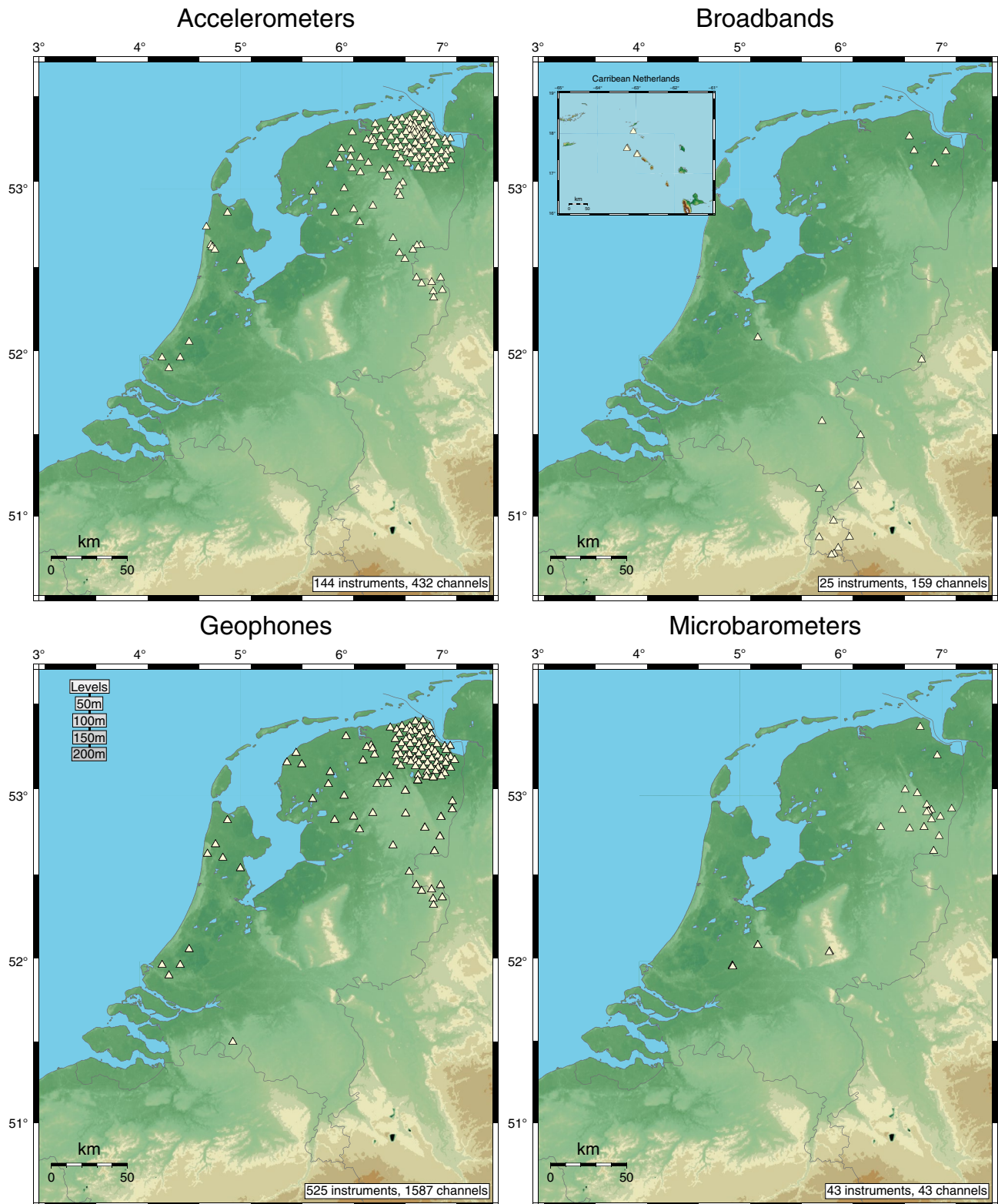


Figure 1. Map of the (Caribbean) Netherlands showing accelerometers, broadband seismometers, geophones, and microbarometers deployed in the Netherlands Seismic-Acoustic Network (NSAN). The network is dense near the Groningen gas field in the north of the Netherlands where geophones are deployed in 200 m deep boreholes at 50 m depth intervals. In October 2020, the network consists of a total number of 728 instruments. Not illustrated are four Global Navigation Satellite System (GNSS) receivers installed on the islands of St. Eustatius and Saba in the Caribbean Netherlands.

techniques and rapidly expanding network densities due to rising interest in, for example, geothermal exploration and large-N networks, data quantities are growing at an increasing rate (e.g., Dost, 1994; Strollo et al., 2020). As mandated by data volumes easily exceeding hundreds of terabytes across data centers and growing beyond tens of terabytes per year, quality verification of data must increasingly rely on automated, trusted, and documented policies and procedures.

Obtaining reliable data from geophysical monitoring infrastructures begins with adequate network design, proper instrument installation and configuration, completeness of metadata, and setting up the necessary infrastructure for reliable telemetry to transfer the recordings to a data center for storage. From there, continuous quality assessment of the incoming data is the backbone to sustain consistent and high data quality standards and create reliable products. The challenges in maintaining an extended and diverse network of geophysical instruments are to verify that (a) the configuration of each instrument in the field is consistent with its metadata, and (b) the performance of the instruments does not degrade over time. Developments toward (automated) geophysical data quality monitoring systems have been made over the last decades, for example, PQLX (McNamara & Boaz, 2006a), MUSTANG (Ahern et al., 2015), DQA (Ringler et al., 2015), WFCatalog (Trani et al., 2017), AutoStatsQ (Petersen et al., 2019), and component ratio monitoring (Pedersen et al., 2020). These systems are often designed to detect and identify data anomalies due to changes in, for example, local site conditions, technical instrumental problems, timing issues, transmission failures, and to reveal inconsistencies in the instrument metadata. Because these problems are inherent to all sensor deployments and exist independently from the instrument in question, similar data quality assessment techniques can be applied for different instruments. Often such anomalies and discrepancies are detected by a researcher, for example, after analyzing a series of earthquake data. A more proactive approach is favorable, and this study presents a system that facilitates the discovery of such potential problems at an early stage based on the comparison of instrumental power spectral density (PSD) estimates against strict quality metrics. Our work extends previous developments in the analysis of PSD estimates for the purpose of quality control by introducing multiple new independent metrics and making recommendations on what metrics to apply to various instruments in a geophysical monitoring network.

The performance of many geophysical instruments can be assessed through a PSD estimate of a segment of its output recording (McNamara & Boaz, 2006b; Rosat et al., 2004). This estimate is a measure of how the power density of the signal is distributed over the full instruments bandwidth. Using estimates of the PSD from different time segments, a probability density function (PPSD) can be aggregated, which introduces a confidence interval on the stochastic PSD estimates. The performance of an instrument can be monitored through the temporal evolution of the PSD, for example, at discrete selected frequencies (De Zeeuw-van Dalfsen et al., 2018), or over its full bandwidth. For example, the PSD estimates of broadband recordings of ground motion are expected to fall within a specific range, for example, the New High (NHNM) and New Low Noise Models (NLNM) derived from global observations (Peterson, 1993). Besides the NHNM and NLNM, alternative statistical bounds are described in the literature, for example, Berger et al. (2004) and Castellaro and Mulargia (2012). Similar confidence intervals have been estimated for accelerometers (Cauzzi & Clinton, 2013) and infrasonic sensors and hydrophones (Brown et al., 2012). These models can serve as a preliminary constraint to verify that the waveform data is recorded within prevalent environmental conditions. Because variations in the PSD can possibly be attributed to local underlying geophysical processes (Burtin et al., 2008; García et al., 2006) global models are often insufficient, and every instrument and site needs to be verified independently. Furthermore, the global models themselves are sensitive to uncertainties introduced by the PSD processing and smoothing that may exceed the uncertainty of the data (Anthony et al., 2020). Therefore, it is recommended that a combination of multiple strategies is used to automatically monitor the performance of geophysical instrumentation when using PSD estimates.

For each instrument constraints are defined on the statistical parameters of the PPSD calculated from the latest month of data based on (a) global noise models from the literature, (b) datalogger quantization noise models following Bennett (1948) and Sleeman (2006), (c) confidence intervals established on manually validated archived waveform data (McNamara et al., 2009), and (d) regionally expected ambient noise characteristics. Datalogger quantization noise models are derived for the network of geophone boreholes and accelerometers in the Dutch province of Groningen where the instruments are configured to measure relatively large ground accelerations without distortion or clipping. As a consequence, the self-noise of the

equipment, which is dominated by digitizer noise, comes close to and at certain frequencies dominates over the ambient noise level. For each sensor and datalogger combination, a model for digitizer quantization noise is derived and used as a theoretical lower limit of the PPSD that can be observed. In addition, for instruments that are expected to be dominated by digitizer noise at low frequencies, the PPSD distribution is expected to fall close to the derived quantization noise level. It is demonstrated that the approach is easily applicable to tiltmeters, despite not being incorporated in the NSAN operational network.

Confidence intervals on the PPSD of incoming data can be derived from an upper and lower percentile of the PPSD of archived and validated data from the same instrument recorded in regular conditions over a full year to encapsulate seasonal variability. These confidence bands represent local low and high-noise models that are distinct for each instrument and site. Additionally, when an instrument records more than just instrumental noise, that is, environmental noise, a scatter is introduced on the stochastic PPSD distribution that is confirmed to be present in the data. Finally, the characteristics of the microseisms are used. In the Netherlands, the spectral peak of the microseisms provides a stable and well-recognizable regional reference for performance monitoring and is used to constrain characteristics of the PSD estimates.

This study focuses on the NSAN, but also demonstrates the approach for geophysical instrumentation that are not presently operated in the monitoring network. In the verification process that is operated weekly, statistical parameters of the latest monthly PPSD of all instruments are compared to these constraints. When an instrument fails to meet these criteria, the station operator is notified about the potential degraded performance of the equipment. The methodology and background to calculate the PSD estimates are described, followed by the database design which is optimized for the storage and retrieval of many PSD estimates efficiently. Next, the spectral constraints devised for accelerometers, geophones, broadband seismometers, microbarometers, gravimeters, tiltmeters, hydrophones, and GNSS receivers are discussed, that are suggested to be applied as quality metrics. Finally, the quality verification procedure operated by the NSAN and its process logic are described, with examples of degraded instrument performance detected by the system. This study is concluded with an operational product for automated data quality assessment for geophysical instruments deployed in the NSAN.

2. Methodology

2.1. Definition of the PSD Estimate

The PSD is calculated by taking the Discrete Fourier Transform (DFT) of a time-variant signal and squaring the magnitude of its complex coefficients, normalizing the power per unit frequency following, for example, Heinzl et al. (2002):

$$PSD(f_m) = 2 \cdot \frac{|y_m|^2}{Nf_s} \quad (1)$$

where f_s represents the instrument sampling frequency, $|y_m|$ the complex modulus of the m^{th} frequency component of the DFT, and N the number of samples used in the DFT. In this convention, the power distribution is mapped to positive frequencies, expressed by the factor 2.

2.2. Systematic Computation of Power Spectral Densities

Despite the publication of the Fast Fourier Transform (FFT; Cooley & Tukey, 1965), the calculation of power spectra remains a computationally intensive task. It is inefficient to load archived data from disk and calculate PSDs on demand for instrumental monitoring purposes and a caching strategy for the PSD segments is recommended. The computational challenge is then shifted toward the storage of millions of spectra and to efficiently retrieve them. Our solution is to store a smoothed and decimated approximation of the PSD estimates using a custom compression scheme that minimizes the storage footprint and offers a flexible and fast retrieval mechanism.

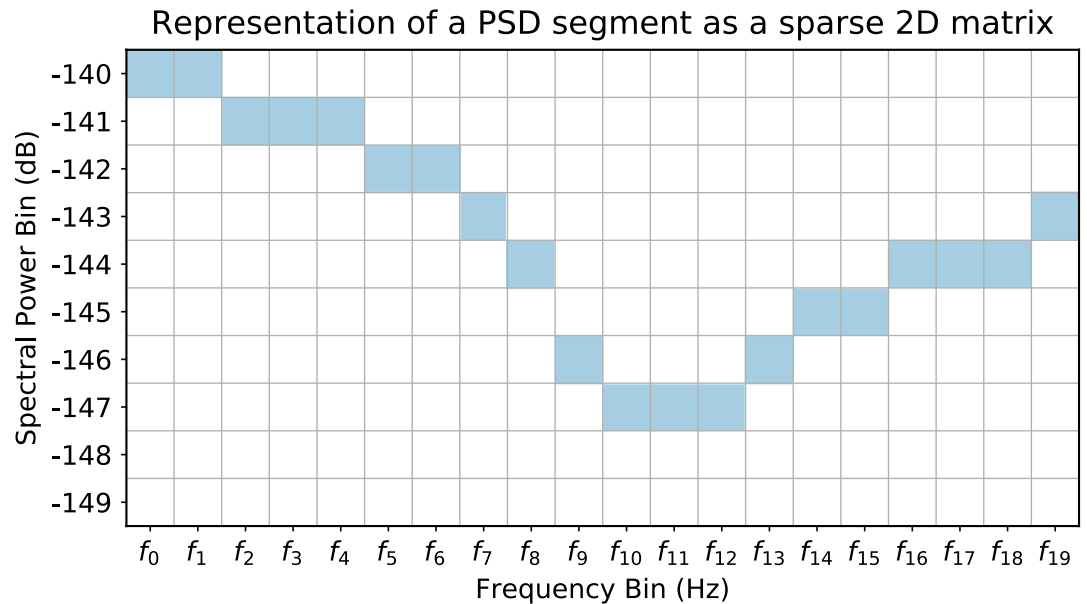


Figure 2. Synthetic power spectral density (PSD) estimate over 20 arbitrary frequency bins. The binned frequencies and corresponding power densities can be treated as a sparse two-dimensional binary matrix. This particular segment only requires a total of 20 bytes to be stored, outside of additional metadata required for full reconstruction.

PSDs are estimated from hourly segments of continuous data with 50% overlap between segments. All data are preprocessed using the Python library ObsPy (Beyreuther et al., 2010) by which overlapping samples in one segment are removed and time-discontinuous data segments are rejected from further processing. The approach of McNamara and Buland (2004) is followed and PSDs are calculated within a predefined fixed frequency range. During the calculation, the hourly waveform segment is split into 13 segments of even length with 75% overlap. For each partial segment, the linear trend is removed and a normalized 10% cosine taper is applied to dampen the effect of spectral leakage caused by discontinuity at the segment edges. The instrument response is evaluated using ObsPy through *evalresp*, and corrected for in the frequency domain to obtain spectral amplitudes in physical units (e.g., m s^{-2} for seismic data). The spectral amplitudes are squared to power and normalized following Equation 1. The 13 resulting PSDs are averaged to obtain the final PSD for that hourly segment following the method of Welch (1967). The averaged PSD of the hourly segment is smoothed over a full-octave band and is expressed in dB and stored for 256 fixed frequencies at one-eighth octave intervals, following the sequence defined in Equation 2, starting at $f_0 = 1,024$ Hz for all instruments. A property of this sequence is that it generates whole integer frequency bin centers at, for example, 1, 2, and 4 Hz commonly used for inspection.

$$2^{-0.125n} \cdot f_0 = [f_0, \dots, 4, \dots, 2, \dots, 1, \dots, f_n] \quad (2)$$

The upper and lower bounds of a frequency bin can be calculated by adding or subtracting half the bin width from its center frequency, respectively. Powers for frequencies above the Nyquist frequency and below the limit that is imposed by the segment length used in the DFT are registered as invalid by a reserved value. The number of selected fixed frequencies in Equation 2 can be chosen arbitrary, but must be large enough to include the low frequencies of interest. The remaining power values are rounded to 1 dB sized bins. The smoothed and decimated approximation of the PSD segment reduces its compressed storage size significantly, and more optimization can be achieved with an appropriate data storage strategy as defined below.

2.3. Storage Strategy

For each segment, the result relates frequency to power at discrete bins that can be represented as a sparse two-dimensional binary matrix, which shape depends on the chosen binning granularity (Figure 2). Because the $\text{PSD}(f)$ relationship is continuously spaced across the frequency domain, and the chosen frequency and

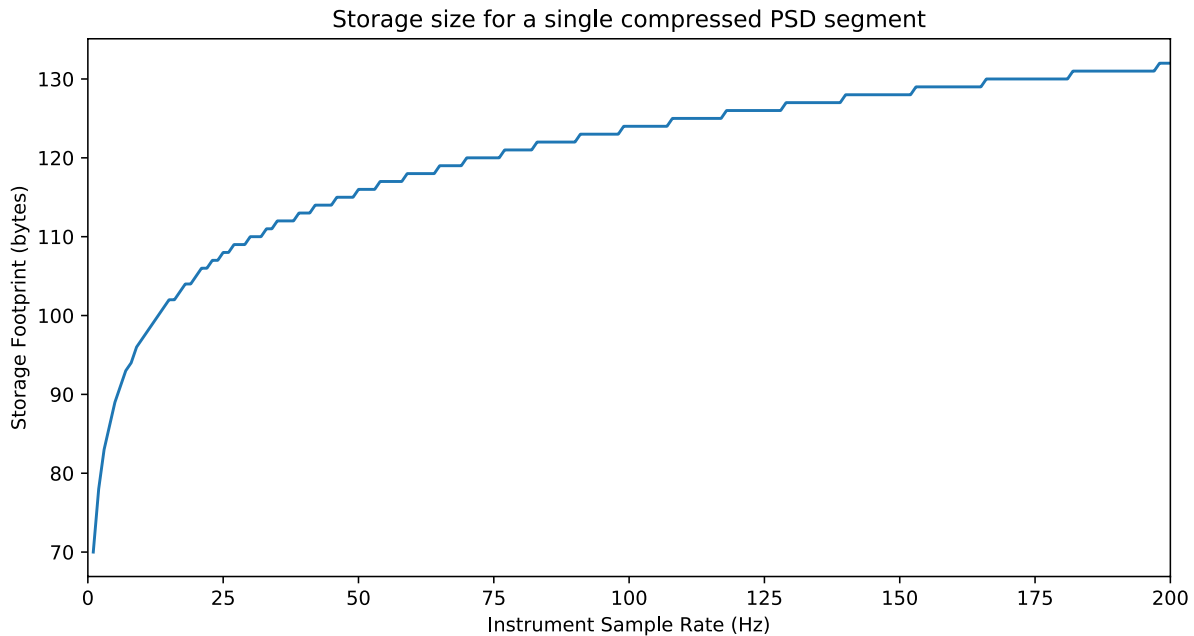


Figure 3. Showing the number of bytes required to store a single power spectral density (PSD) array binned at 1 dB and one-eighth octave bins within the fixed frequency range defined in Equation 2. The number of valid frequencies is limited by the Nyquist frequency of the instrument and the chosen segment length for the Discrete Fourier Transform (DFT). The relationship between the instrument sample rate and required storage is logarithmic.

amplitude bins are equivalent for all segments, the full spectrum can thus be represented as a contiguous one-dimensional array of PSD values, with the associated frequencies implicitly following the sequence defined in Equation 2.

Invalid powers for frequencies that are beyond the Nyquist frequency are eliminated from the start of the array, and the index of the first valid frequency (f_{offset}) is stored auxiliary to the array so that the spectrum can be reassembled. Power values for low frequencies beyond the segment length will truncate the array to the lowest valid frequency and simply reduce its length. Most currently available recordings are digitized with 24 bits which results in a dynamic range that is smaller than 150 dB. When the power densities are rounded to whole integer dB units the difference between the minimum and maximum value fits within a single-byte integer. This property enables a shift of the PSD by an integer PSD_{shift} that brings all power values to the positive range, and is stored as metadata to the array. A single PSD segment can thus be represented as an array of 8-bit unsigned integers composed as follows:

$$\text{UInt8Array} = [PSD_{f_{\text{offset}}}, PSD_{f_{\text{offset}+1}}, \dots, PSD_{f_{\text{offset}+N}}]_{\text{uint8}} \quad (3)$$

where N represents the number of valid frequencies that is a function of the instrument Nyquist frequency and thus the sampling interval. Following this method, the PSD of a single segment, even at high sampling rate, can be represented with a small storage footprint (Figure 3). This size excludes the size of the metadata required to identify the segment within the database, including the offset (f_{offset}) and shift (PSD_{shift}) required for reconstruction.

2.4. Database Selection

The derived PSD segments are stored in a database with metadata that describes its time coverage and the seismological standard SEED data stream identifier (Ahern et al., 2007). This metadata is indexed and used to retrieve the spectra that satisfy particular search criteria for, for example, a specific instrument and time span. A checksum of the raw waveform data and metadata are included to detect changes in the (meta)data that mandates the reprocessing of PSD segments in the database.

Several technical solutions were explored for the storage of millions of PSD segments, accounting for the way the database will be used. Due to the inherent variability of individual PSD estimates, the PPSD is used to represent a statistical distribution of multiple PSD estimates. The objective of aggregating individual binned PSD segments to a PPSD is equivalent to generating a two-dimensional histogram (PSD, f) that is accumulated over a third temporal dimension (t), namely the PSD segments over time. Initially, SciDB was tried (Stonebraker et al., 2013) as it is designed for array and matrix operations of this kind. One large challenge was encountered as arrays are expected to have a predefined size, which conflicted with a continuously growing number of PSD segments over time. The ObsPy library offers a method to calculate PPSDs and save them using NumPy (Van Der Walt et al., 2011) compressed files. This approach has a storage footprint that is orders of magnitude larger than our custom compression scheme and was therefore not used. The NoSQL database MongoDB became the storage database of choice, as the schema-less nature of this database facilitates rapid prototyping and quickly evolved into a functional product. Alternatively, a Relational Database Management System (RDBMS; e.g., MySQL, MariaDB, PostgreSQL) can be chosen with no significant effect on the database performance. The compression scheme presented in this study keeps the spectral database of the current waveform archive (100 TB) at a manageable size of roughly 30 GB, which is about 0.03% of the raw data volume.

2.5. Aggregation to Probabilistic Power Spectral Densities

On top of the spectral database an Application Programming Interface (API) was developed to find and access the PSD estimates and aggregate the results. When an API request is made, the PSD segments that match the request criteria (e.g., temporal coverage, or that for a particular SEED identifier) are returned. These segments are passed to a subroutine that allocates an empty zero-filled matrix of dimensions $255 \times 256 (N_p \times N_f)$ that corresponds to the number of selected power and frequency bins, respectively. For every PSD segment, the array of 8-bit unsigned integer values are unpacked and used to find the respective cells within the matrix to be incremented, where invalid values are discarded. The frequency bin can be calculated from its frequency offset (f_{offset}), in combination with its particular index in the array. The power value is represented by the unsigned byte value corrected for by the power shift (PSD_{shift}) value. When all spectra have been aggregated the resulting matrix is divided element-wise by the total number of segments used to convert the absolute values to probability of occurrence. The resulting histogram then represents a fully reconstructed PPSD for the requested options and can be returned to the client for further analysis.

3. Automating PSD Quality Control for the NSAN

Extensive and precise quality control of data is one of the most vital and resource intensive tasks of a data center. The large quantity of incoming geophysical data from the NSAN requires that the process of quality control becomes increasingly automated. The operational procedure includes all types of instruments and divides them into three distinctive processing stages. Stage (0) includes instruments in the first month of operation and serves to validate whether the instrument performs well enough to be moved into production. Stage (1) contains the set of instruments in the first year of operation until one year of high quality data is available and the instrument proceeds to the following stage. Stage (2) enforces the guarantee that the quality of an instrument does not degrade over time by comparing incoming data to a history of manually validated data that was archived during stage one of the instruments deployment.

3.1. Instrument Performance Criteria

Power spectra can be utilized as a quality metric as the distribution of power over frequency generally falls within an expected range depending on ambient noise conditions and intrinsic instrumental noise. In the following sections the recommended PPSD criteria for many geophysical instruments are defined and discussed that can be applied as a performance metric. In the NSAN, the latest monthly PPSD of all instrumental channels are automatically verified in weekly intervals against these criteria. If one of the metrics fails, the station operator is notified of the suspected degraded instrument performance. Geophysical

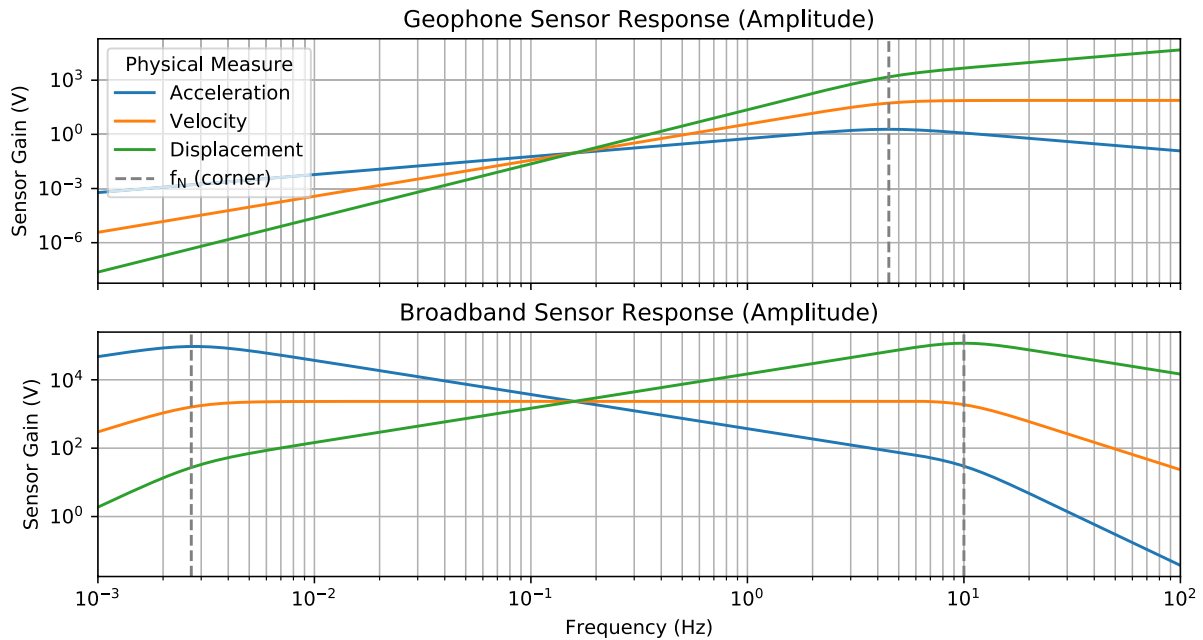


Figure 4. Examples of frequency-dependent sensor gain. (Top) sensor gain in V for a geophone with a resonant frequency of 4.5 Hz, a damping factor of 0.702, and an effective generator constant G_e of $75.8 \text{ V m}^{-1} \text{ s}^{-1}$. The amplitude of the frequency response to ground displacement (green), velocity (orange), and acceleration (blue) is shown. The sensitivity of geophones to ground acceleration decays around its resonant frequency f_0 indicated by the vertical gray line. (Bottom) sensor gain for an STS-1 broadband station with a G_e of $2,332 \text{ V m}^{-1} \text{ s}^{-1}$, corner frequencies of $f_0 = 360 \text{ s}$ and $f_1 = 10 \text{ Hz}$, and damping factors $h_0 = 0.707$ and $h_1 = 0.623$. The broadband station is much more sensitive to ground displacements at low frequencies compared to a geophone. An accelerometer has a flat response to ground acceleration below its resonant frequency and is therefore not shown.

instruments that are not part of the NSAN operational network are discussed and it is demonstrated how these instruments can be easily integrated in the future.

3.1.1. Quantization Noise Constraint

Geophysical monitoring infrastructures consist of many different types of sensors and dataloggers, and the combination of the two is referred to as an instrument. The dynamic range of an instrument is determined by the ratio of the maximum to minimum amplitude of a signal that can be recorded and can be limited by either the sensor or datalogger (Steim, 2015). The maximum amplitude is usually defined by the clip level of the sensor, whereas the minimum amplitude is often limited by self-noise of the digitizer. An expression for the self-noise of the system thus provides a constraint on the minimum PSD level that can be expected in any output recording.

For ground motion data, the instrumental noise is expressed in terms of ground acceleration power density ($\text{m}^2 \text{ s}^{-4} \text{ Hz}^{-1}$). The maximum sensor amplitude (i.e., clip level) A must thus be expressed in terms of ground acceleration too. This amplitude is constant for accelerometers, that is, a flat frequency response, and frequency dependent for, for example, geophones and broadband seismometers (Figure 4). The frequency band for the quantization noise constraint is defined between 0.033 Hz and 80% of the instrument Nyquist frequency. The self-noise models are inaccurate near the Nyquist frequency where the effects of anti-aliasing filters play a significant role in decreasing the instrument sensitivity (Sleeman, 2006), and at low frequencies due to instabilities caused by tilt, wind, pressure, and temperature variations.

Analog-to-digital converters (ADC) discretize continuous functions to quantization levels, and in this process, truncation errors to the nearest quantization level are introduced. Bennett (1948) derived an equation for the quantization noise power of an ADC over a full-load sine wave:

$$\epsilon_{\text{rms}}^2 = \frac{\Delta^2}{12} \quad (4)$$

where Δ is the digitizer resolution or quantization interval which can be expressed as $2A / 2^n$ with n the number of effective bits of the digitizer, and A the full-load amplitude. Despite the assumption of a full-load sine wave input, this equation appears to hold for sufficiently complex signals passing over many quantization intervals (Oppenheim & Schaffer, 2009). For a white noise spectrum the power density is constant over the full bandwidth. This means that the PSD of the quantization error can be estimated as the mean square error ϵ_{rms}^2 derived in Equation 4 replaces $|y_m|^2$ over N in Equation 1 following Parseval's theorem:

$$PSD_{\text{min}} = 2 \cdot \frac{\epsilon_{\text{rms}}^2}{f_s} \quad (5)$$

Equation 5 can be expanded using Equation 4, rewritten, and expressed in dB relative to a reference value of $1 \text{ m}^2 \text{ s}^{-4} \text{ Hz}^{-1}$ for ground motion instruments.

$$PSD_{\text{min}} = 10 \log_{10} \left(\frac{T}{6} \left(\frac{2A}{2^n} \right)^2 \right) \quad (6)$$

Equation 6 describes an absolute minimum white noise spectrum that is uniform over all frequencies. This level depends on the sampling interval T (f_s^{-1}), as the total noise power does not change with a different number of samples per second, effectively reducing the PSD (Oppenheim & Schaffer, 2009; Sleeman, 2006).

Inside active electronic components the electronic noise level is inversely proportional to frequency. This f^{-1} type of noise dominates the power spectrum at low frequencies. Following Sleeman (2006), $PSD_{\text{min}}(f)$ is expressed, now a function of frequency, as a superposition of the flat white noise spectrum defined in Equation 6 and a frequency-dependent pink noise spectrum. This model assumes that the frequency-dependent noise is thus proportional to f^{-1} , which often holds for instruments in the NSAN, but is not a universally valid assumption under all circumstances.

$$PSD_{\text{min}}(f) = 10 \log_{10} \left(\frac{T}{6} \left(\frac{2A}{2^{n_1}} \right)^2 + \frac{T}{6f} \left(\frac{2A}{2^{n_2}} \right)^2 \right) \quad (7)$$

where n_1 and n_2 represent the effective number of bits for each spectrum, respectively. From experience with instruments deployed in the NASN, it is found that the value of n_2 is related to n_1 following $n_2 = n_1 + 1$. This eliminates one unknown and combines both number of effective bits into a single variable number of proxybits η . When the sampling interval T is also implicitly included in the number of unknown proxybits η , Equation 7 can be reduced and rewritten to:

$$PSD_{\text{min}}(f) = 10 \log_{10} \left(\frac{1}{6} \left(\frac{2A}{2^\eta} \right)^2 \left(1 + \frac{1}{4f} \right) \right) \quad (8)$$

For every datalogger and sensor combination, the single unknown variable η is estimated by fitting it to an instrument that is dominated by self-noise over part of its bandwidth, generally at frequencies below 1 Hz where f^{-1} noise dominates. The exact value of η must be close to the number of bits provided by the digitizer manufacturer but depends on the (noise) specifications of the instrument and the configured internal (over) sampling interval of the datalogger. This constraint is determined once, and then applied to other instruments of the same type. The minimum of the PPSD may under no circumstances fall below this theoretical baseline. The results for all types of instruments in the NSAN are compiled in Table 1, and details on the methodology per instrument type is discussed in Section 3.2.

3.1.2. Global Noise Model Constraint

For highly sensitive instruments (e.g., broadband seismometers and gravimeters), the level of ambient noise usually exceeds that of quantization noise, and a generic global noise model is more suitably chosen as a lower limit. One example is the Peterson (1993) global noise model that includes long period disturbances, microseisms, and anthropogenic noise. Instruments installed in a high-noise environment may produce

Table 1

Compilation of Different Accelerometers and Geophones Deployed in the NSAN and the Parameters Used to Calculate the Instrumental Lower Noise Bounds

Instrument	A (m s^{-2})	V_{sensor}	$V_{\text{datalogger}}$	η
Batch-1 accelerometers	4g	± 20	± 20	24.7
Batch-2 accelerometers	2g	± 5	± 20	22.7
Batch-3 accelerometers	2g	± 20	± 20	24.7
Batch-4 accelerometers	2g	± 5	± 5	24.7
Etna-2 accelerometers	2g	± 2.5	± 2.5	24.5
SM6 geophones	f -dependent	± 2.5	± 2.5	24.3
SM6H geophones	f -dependent	± 2.5	± 2.5	24.3

Note. All instruments sample at 200 Hz. A represents the maximum amplitude that may be frequency dependent, V_{sensor} and $V_{\text{datalogger}}$ the sensor output voltage and datalogger input voltages, respectively. A list of all instruments per group can be found in Table S1. The Difference in the estimated proxybits between Batch-2 and Batch-3 accelerometers emerges from a different setting between the configured sensor output voltage range between -5 and 5 V and expected digitizer input voltage between -20 and 20 V. This inconsistency in the instrument configuration introduces a range of factor four that is never digitized, effectively not using two available bits on the datalogger.

Abbreviation: NSAN, Netherlands Seismic-Acoustic Network.

PSDs above the NHHM, whereas the PSD of instruments installed in quiet ambient conditions sites may fall near the NLNM. These models are based on observations from broadband instruments and therefore the NLNM does not translate well to strong motion accelerometers (Cauzzi & Clinton, 2013) and geophones, of which many are installed in the NSAN. The International Data Centre (IDC) provides similar noise models for acoustic and hydroacoustic data (Brown et al., 2012). The median of the monthly latest PPSD of an instrument should fall within its respective global noise model from the literature and constrains the PPSD over a large bandwidth.

3.1.3. Microseisms Constraint

Oceanic wave-wave interaction and coastal swell imposes a distinctive and reliable noise field over the Netherlands that is limited to a certain frequency band (Kimman et al., 2012). These microseisms serve a stable minimum and maximum constraint on the expected level of ambient noise at the instrument site. The geographical extent of this field is frequency dependent, but frequencies of $f \approx 0.3$ Hz attenuate less than higher frequencies and thus can be observed consistently across the Netherlands, even at depths down to 200 m depth by geophones in boreholes (Figure 5). The minimum and maximum expected power at $f \approx 0.3$ Hz was constrained over a full year at monthly intervals with 3σ confidence intervals for various distances from the coast as illustrated in Figure 6.

Despite a clear relationship between the observed PSD around the secondary microseism frequency and distance to an active coastal area can be recognized, a single minimum and maximum for the entire Netherlands is used. The expected noise power in the Netherlands at $f \approx 0.3$ Hz appears limited between PSD_{max} at -90 dB and PSD_{min} at -140 dB. These two values provide a constraint for the expected level of the microseism at 0.3 Hz specifically for the Netherlands.

3.1.4. Low-Frequency Constraint

This threshold is suggested for accelerometers and geophones at $f = 0.025$ Hz where the PSD is expected to be dominated by quantization noise. As the probabilistic distribution over these frequencies is narrow in this range, it is expected that the median of the power spectrum falls within the theoretically derived PSD_{min} from Equation 8 and $PSD_{\text{min}} + 10$ dB.

3.1.5. Minimum-Maximum Difference Constraint

This threshold is introduced in order to detect broken sensors, or instruments for which the sensor is not (properly) connected to the digitizer. In these cases only instrumental noise is recorded. In normal conditions, the difference between the statistical minimum (2.5^{th}) and maximum (97.5^{th}) percentile of the PPSD

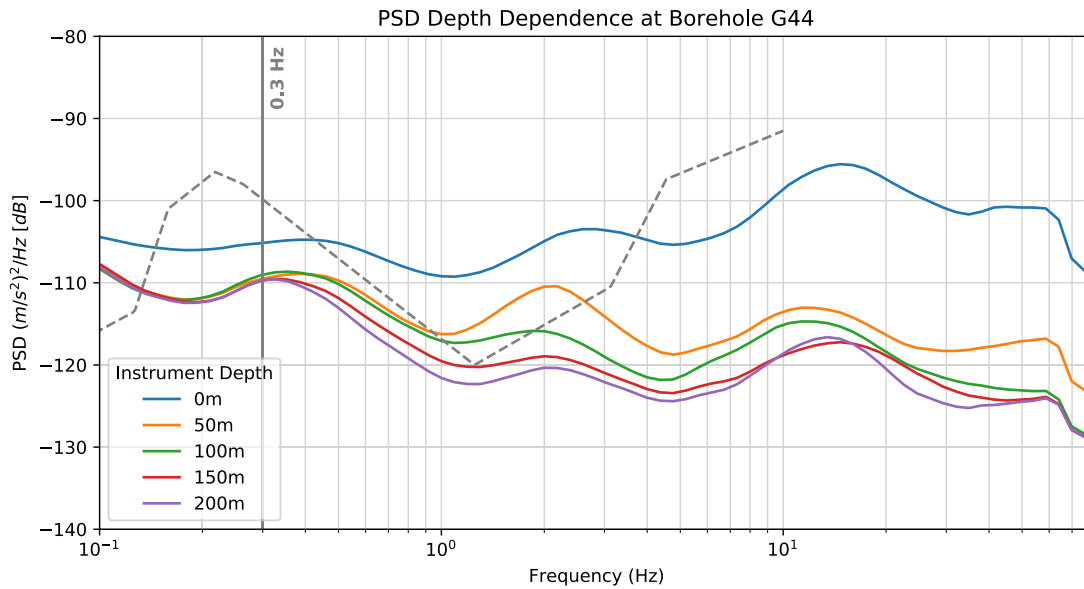


Figure 5. Showing the averaged and smoothed power spectral density (PSD) over 2019 of instruments G440 (surface accelerometer) and G441-G444 (geophones) deployed at 50 m depth intervals, respectively. Noise at higher frequencies attenuates faster than lower frequencies with increasing depth. The noise power through all depth levels is near each other around 0.3 Hz. The surface accelerometer is influenced by tilt and atmospheric variations and always expresses higher noise levels when averaged over a full year. The New High Noise Model (NHNM) after (Peterson, 1993) is shown for reference.

over a month at $f \approx 3$ Hz must display at least a typical scatter of 5 dB. This frequency is chosen because it falls in the bandwidth of anthropogenic noise where a large variance in the PSD estimates is expected. If this difference is smaller than 5 dB, a warning is issued that the instrument might be dysfunctional. False positives of this constraint have been identified in the system for functional instruments operating in very quiet conditions.

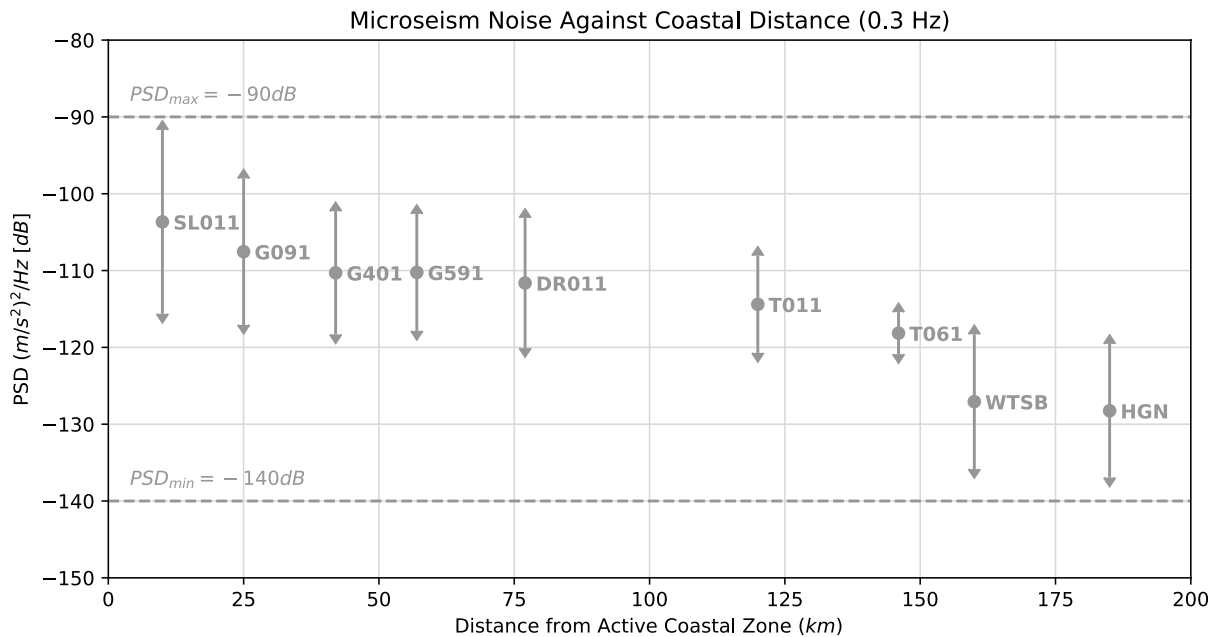


Figure 6. The power spectral density (PSD) at 0.3 Hz, as a function of distance from the (active) coast. The round markers indicate the average levels over one year of data from the labeled station, the bars illustrate the -3σ and $+3\sigma$ region (99.7% confidence region). From this distribution of PSD levels, the microseism constraint is derived, yielding at 0.3 Hz a PSD_{min} of -140 dB and a PSD_{max} of -90 dB.

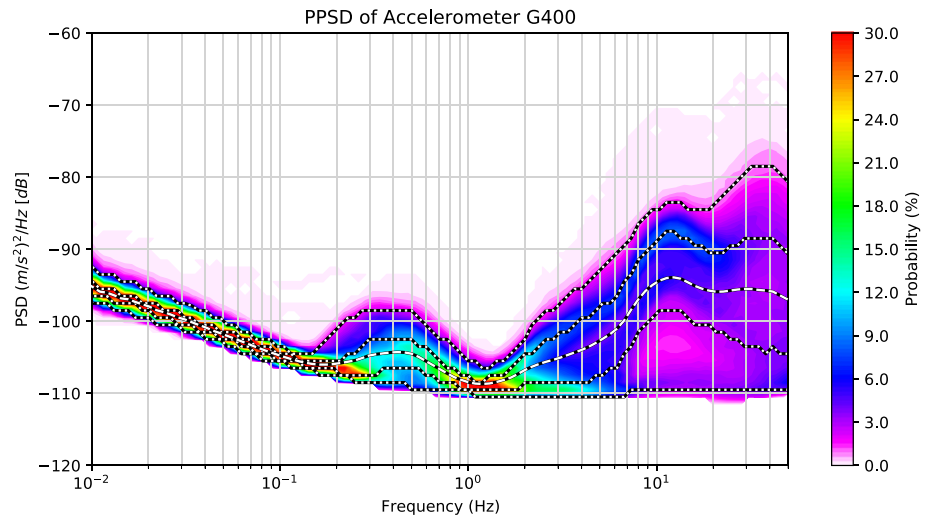


Figure 7. Showing the probability density function (PPSD) of surface accelerometer G400 (vertical) with the 50th (median; dashed), 2.5th, 25th, 75th, and 97.5th percentiles (dotted) projected on the PPSD.

3.1.6. Default Bound Constraint

The default bound comparison comprises a check against a constant upper and lower default bound of -80 and -140 dB, respectively, for seismic instruments. These wide bounds are based on best estimates for the Netherlands from experience and have no physical background but should identify large anomalies at any frequency.

3.1.7. Percentile Constraint

The percentile constraint has been previously applied by, for example, Ringler et al. (2015) and is the most effective metric that is placed on instruments that have been deployed for over a year and have an archived record of manually verified high quality data. For each instrument, from archived PSD estimates stored in the database an upper (2.5th) and lower (97.5th) percentile curve is computed. These data-driven bounds represent confidence limits for incoming data, within average environmental and instrumental noise for that particular instrument and location. Every week, the median of the latest monthly PPSD is compared against these statistical constraints, and when a threshold is crossed, the deviation may be caused by degraded instrument performance over time. Crossing of the bounds may also be caused by the addition or removal of a strong persistent source of noise. The sensitivity of the detection can be tuned by choosing a particular percentile limit (Figure 7). Furthermore, both the mean and median of the PPSD can be used as a trigger, where using the median will decrease the sensitivity toward single large anomalies.

3.2. Quality Assessment of Geophysical Instruments

3.2.1. Accelerometers

Most accelerometers in the NSAN are of type EpiSensor (Kinometrics) with a dynamic range of 155 dB and a clip level of 2 or 4 g. The instruments sample ground acceleration at sampling rates of 200 Hz using 24-bit dataloggers. Accelerometers are characterized by a flat response to acceleration below their resonant frequency. Because the instrument is dominated by instrumental noise over part of its bandwidth, a lower limit imposed by quantization noise can be empirically derived. The maximum amplitude A expressed with respect to ground acceleration is thus equivalent to an accelerometers clip level, and can therefore be inserted in Equation 8 as a constant. The f^{-1} component is found by fitting Equation 8 to data to estimate the number of proxybits η as illustrated in Figure 8, resulting in an estimate of $\eta = 22.7$ for that particular instrument.

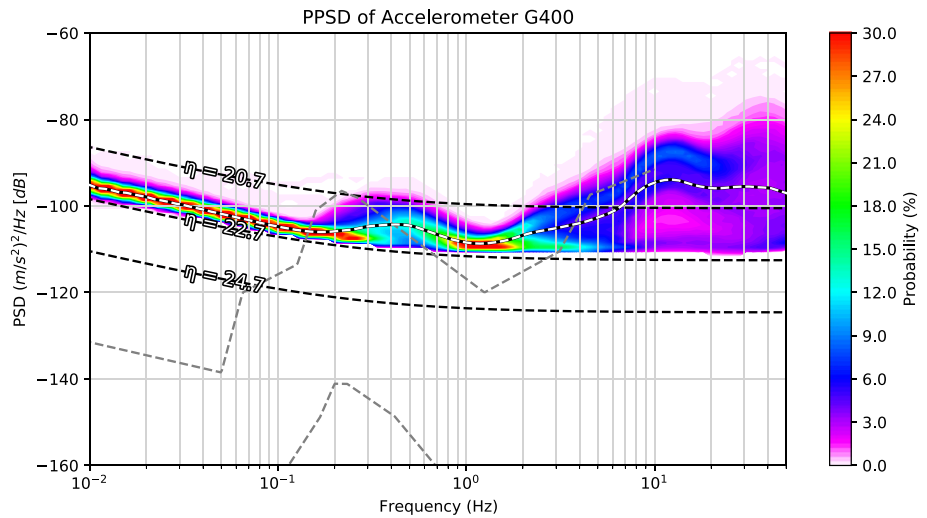


Figure 8. Probability density function (PPSD) of surface Batch-2 accelerometer G400 (vertical). The median value of the PPSD is illustrated by the dotted white line. Curves for various proxybits η following Equation 8 are shown. For this example, a value for $\eta = 22.7$ is found and used to model the digitizer quantization noise of this instrument and all other instruments with the same setup (Table 1).

3.2.2. Geophones

Geophones are passive velocity transducers and generally have a flat velocity response above its resonant frequency f_0 (Figure 4). Below this frequency, the sensitivity decays proportional to a nominal damping factor h as described by, for example, Havskov and Alguacil (2016) and can be expressed in terms of ground acceleration:

$$T_a^v(\omega) = G_e \frac{-i\omega}{\omega_0^2 - \omega^2 + 2i\omega\omega_0 h} \quad (9)$$

where G_e is the effective instrument generator constant in $V/m \text{ s}^{-1}$, ω and ω_0 are the angular and resonant frequency, respectively. The maximum amplitude A expressed as acceleration is found by dividing the maximum sensor output voltage V_{\max} by the complex modulus of the frequency-dependent sensitivity as defined in Equation 9:

$$A(f) = \frac{V_{\max}}{|T_a^v(\omega)|} \quad (10)$$

The frequency-dependent amplitude $A(f)$ for geophones expressed in acceleration can be applied in Equation 8, and used to estimate η following an identical approach as demonstrated for accelerometers. Examples for station T064 for various proxybits η are illustrated in Figure 9, where the number of $\eta = 24.3$ is empirically recovered.

3.2.3. Broadband Seismometers

Broadband seismometers remain sensitive to ground accelerations at low frequencies, yet not to direct components at zero frequency (Figure 4). The STS-1 sensors installed in the network have a flat response to ground velocity between 360 s and 10 Hz. The high sensitivity of the sensor limits the maximum ground acceleration that can be measured by the seismometer before clipping. This suggests that for dataloggers with input that is (a) aligned with the maximum sensor output without distortion, and (b) have a large dynamic range (>140 dB) may have quantization noise below the ambient noise (Figure 10). For an STS-1, because of its lower and upper corner frequency the response is expressed as Equation 9 multiplied by an extra term (Dost & Haak, 2002):

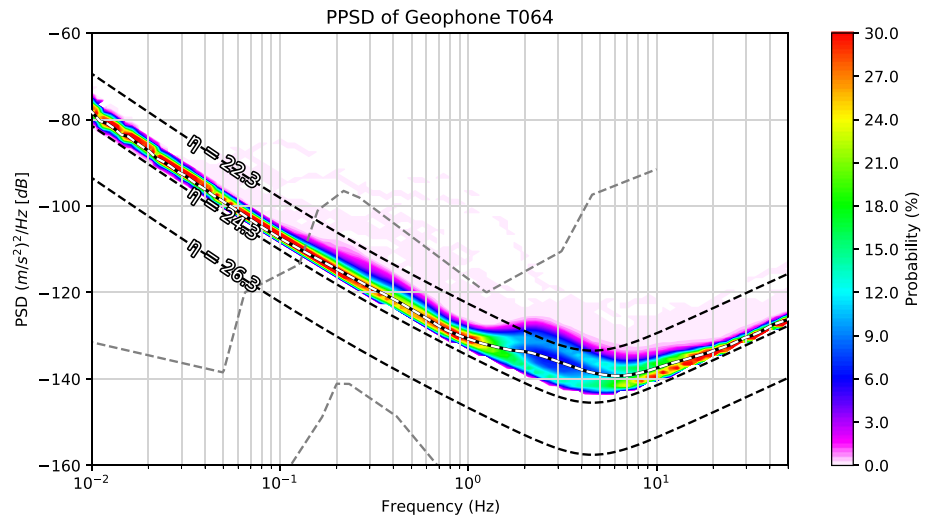


Figure 9. Probability density function (PPSD) of borehole SM6H geophone T064 (vertical) at 200 m depth. The median value of the PPSD is illustrated by the dashed white line. Curves for various proxybits η following Equations 8–10 are shown. For this example, a value of $\eta = 24.3$ is found and used to model the instrumental lower noise limit of this instrument and all other instruments with the same setup (Table 1).

$$T_a^v(\omega) = G_e \frac{-i\omega}{\omega_0^2 - \omega^2 + 2i\omega\omega_0h_0} \cdot \frac{\omega_1^2}{\omega_1^2 - \omega^2 + 2i\omega\omega_1h_1} \quad (11)$$

where the indices represent the natural damping h_i and frequency ω_i of the lower (0) and upper (1) corner, respectively (Figure 4). The theoretical curves for two proxybits η are shown in Figure 10 and confirm that the limit falls below that of environmental noise. The presented equations are different for STS-2 (Dost & Haak, 2002) or STS-5 sensors and depend on the generation of the electronics, but the conclusion remains unchanged. A quantization noise model is not effective when it falls below a seismic noise model for the entire bandwidth of interest. For broadband seismometers the Peterson (1993) NLNM sets a stricter and more useful lower limit.

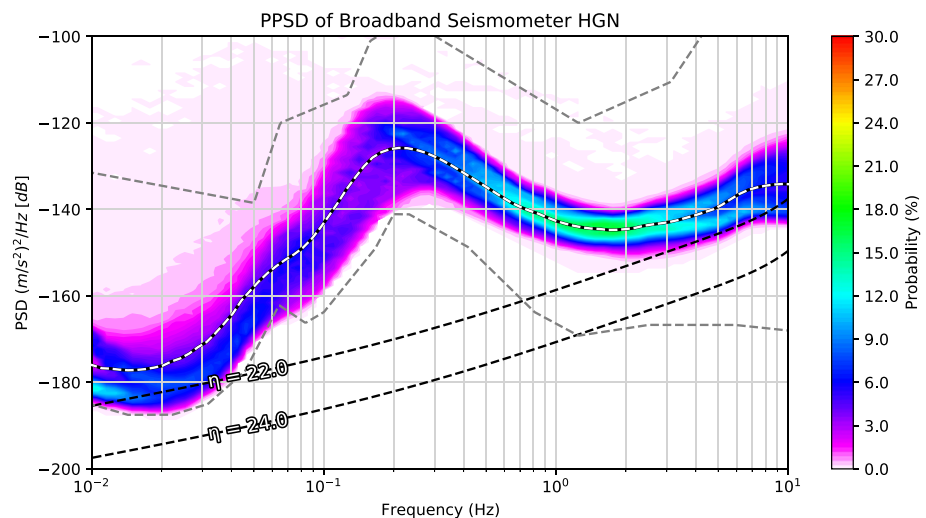


Figure 10. Probability density function (PPSD) of STS-1 broadband station HGN (vertical). The theoretical quantization noise of a datalogger for $\eta = 24.0$ is shown. From the data alone it is impossible to fit a model of quantization noise. Even at very low frequencies, electronic f^{-1} noise does not overtake the ambient noise signal. The quantization noise model has no added value, and a stricter measure for the expected lower limit of noise over the full bandwidth is the Peterson (1993) New Low Noise Model (NLNM), illustrated in dashed gray.

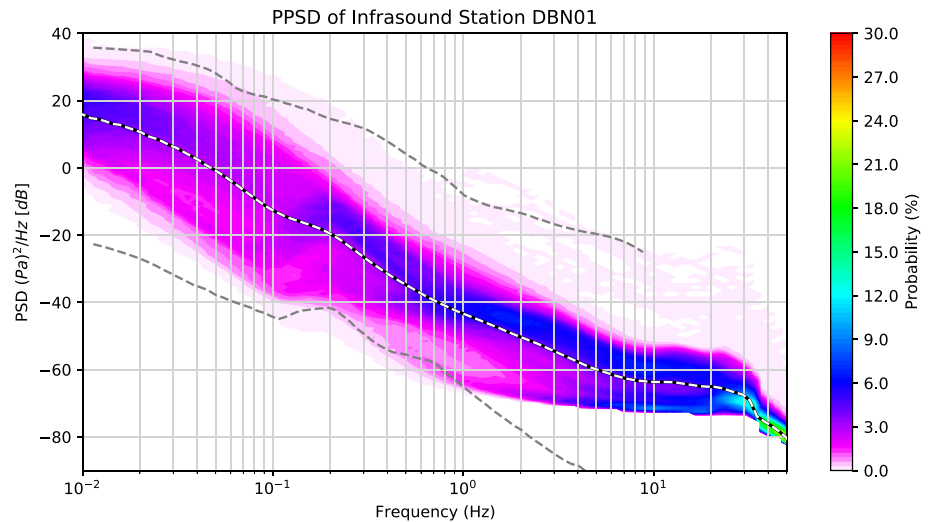


Figure 11. Probability density function (PPSD) of infrasound station DBN01 deployed at the Royal Netherlands Meteorological Institute (KNMI) for 2019 using a segment length of 1 h using a reference of $1 \text{ Pa}^2 \text{ Hz}^{-1}$. There is a large seasonal variability in the noise characteristics of the atmosphere, leading to a scattered power spectral density (PSD) distribution. The International Data Centre (IDC) Infrasound Global High and Low Noise Models (Brown et al., 2012) are illustrated in dashed gray.

3.2.4. Microbarometers

The sensitivity of KNMI microbarometers (Mentink & Evers, 2011) to pressure is roughly flat throughout the frequency spectrum of interest. The dynamic range of the instruments is limited by the sensor at 100 dB, while the 24-bit dataloggers yield a dynamic range in the order of 146 dB, prohibiting a fit for quantization noise. Furthermore, the ambient atmospheric noise also clearly exceeds the expected f^{-1} noise of 10 dB per decade, and thus a more reliable measure for the expected lower limit of noise over the full bandwidth is the IDC Infrasound Global High and Low Noise Models (Brown et al., 2012) illustrated in Figure 11.

3.2.5. Hydrophones

Hydrophones are not employed in the NSAN, and the PSD processing is done similarly to that of infrasound stations, but the response of a hydrophone to pressure usually decreases with lower frequencies. It is challenging to determine an empirical noise model because the mechanical transfer functions of the instruments are more complex compared to seismometers. Instead, for demonstrative purposes the poles and zeros are evaluated from the metadata to obtain the precise instrument transfer function. However, this makes the analysis practically useless since one goal of this criteria is to detect inconsistencies with the instrument metadata in the first place. The simplified quantization and electrical noise model derived in Equation 8 does not hold well for the combination of the rising and flat part of the noise spectra (Figure 12). The slope of the f^{-1} electronic noise fits well with the data, however, a more suitable model is one with more degrees of freedom (Sleeman, 2006). In any case, the IDC Hydroacoustic Global High and Low Noise Models (Brown et al., 2012) provide a much tighter constraint and will generally always fall above any fitted quantization noise model, rendering the digitizer quantization noise constraint redundant.

3.2.6. Tiltmeters

Tiltmeters are commonly used in monitoring infrastructures on the flanks of active volcanoes to detect periods of surface deformation caused by, for example, periods of inflation and deflation (Dzurisin, 2003). The added value of observations from tiltmeters was explored in monitoring the Alkmaar gas field for subsurface deformation induced by pressure variations in the gas reservoir back in the end of the 20th century (Sleeman et al., 2000). The instruments are no longer in use in favor of a dense network of geophones and accelerometers. The working mechanism behind the tiltmeter is similar to the principle of an accelerometer, but instead of measuring ground motion it records the angle between the vertical component of gravity and the surface normal of the instrument. This measurement was historically done using a pendulum, but

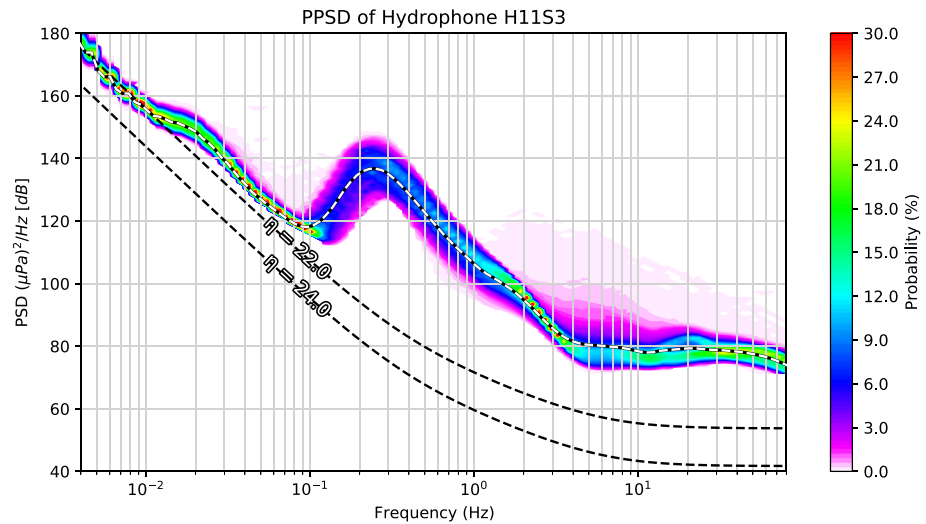


Figure 12. Probability density function (PPSD) of hydrophone H11S3 deployed in the network of International Miscellaneous Stations (IMS). The hydrophone is of type High-Tec HTI-90-U and processed with a segment length of 1 h using a reference of $1 \mu\text{Pa}^2 \text{Hz}^{-1}$. The instrument response is evaluated using the poles and zeros information from the metadata, using a maximum voltage of 3.2768 V as specified by the manufacturer of the data acquisition system.

in modern tiltmeters the most accurate measurement is accomplished through an optical bubble level. Inside tiltmeters, the equivalence principle states that a tilt of θ radians provides an identical record as a horizontal acceleration of:

$$a(t) = g \tan(\theta(t)) \quad (12)$$

where g is the local gravitational acceleration ($\approx 9.81 \text{ m s}^{-2}$ in the continental Netherlands). Using Equation 12, the observed tilt in radians is converted to a virtual horizontal acceleration (Figure 13). The instrument response is flat to acceleration, and the maximum amplitude A is specified by the manufacturer data-sheet at $330 \mu\text{rad}$. A theoretical quantization noise model can be fitted using Equation 8 using a flat response to ground acceleration resulting in to $\eta = 17.0$, closely matching the specification of the manufacturer of the

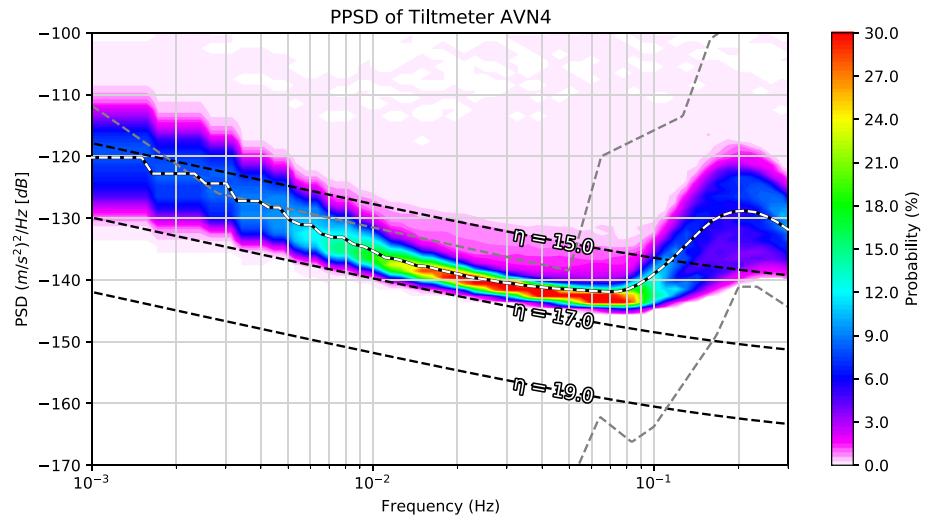


Figure 13. Probability density function (PPSD) of Applied Geomechanics LILY Tiltmeter (Serial Number: 8209) deployed in Oklahoma for 2019 using a segment length of 1 h. The Peterson (1993) noise models are illustrated in dashed gray. The number of fitted proxybits η comes out to approximately 17.0.

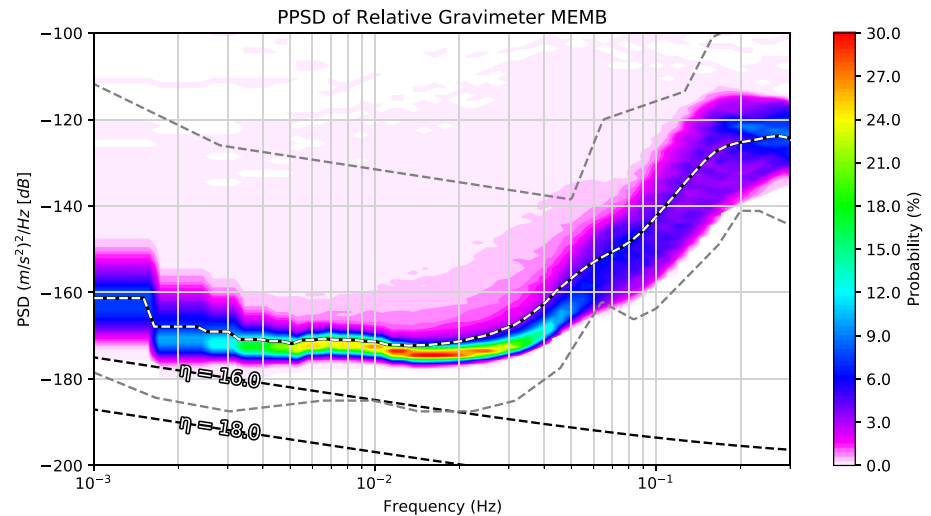


Figure 14. Probability density function (PPSD) of station MEMB (GWR C021 iGrav) superconducting gravimeter deployed in Membach, Belgium for 2019. The data have been corrected for the instrument acceleration frequency response over its full bandwidth. The white dashed line is the median of the PPSD. The quantization noise model from Equation 8 with two values for proxybits η is shown in black, where the internal analog-to-digital converter (ADC) has 24 available bits. The Peterson (1993) noise models are illustrated in dashed gray.

internal 16-bit datalogger. The microseisms are clearly observable in the instrument too and is also recommended to be used as a constraint on the median of the PPSD.

3.2.7. Relative Gravimeters

At present, the NSAN does not employ gravimeters for geophysical monitoring in its operational infrastructure, but acknowledges the potential for, for example, volcano monitoring in the Caribbean Netherlands, similar to what is being explored in the NEWTON-g project (Carbone et al., 2020; Ménoret et al., 2018; Middlemiss et al., 2016), or for hydrothermal monitoring purposes (Sugihara & Ishido, 2008).

The working principle behind the relative mechanical spring gravimeter is identical to that of an accelerometer, and superconducting gravimeters work by the levitation of a niobium sphere in a stable persistent magnetic field, creating a virtual non-mechanical mass-on-spring system (Van Camp et al., 2017). Compared to accelerometers, gravimeters are designed with a lower resonant frequency and are thus characterized by a much higher sensitivity (Havskov & Alguacil, 2016). Its transfer function is flat to acceleration except the sensitivity drops proportional to ω^{-2} above the resonant frequency. The high sensitivity of the gravimeter at low seismic frequencies makes it easily saturated by, for example, surface waves from seismic events.

Compared to seismometers, for gravimeters it is less common to publish experimental transfer function estimates and generally a single flat sensitivity is used. This sensitivity is generally sufficient for the study of low frequencies signals (e.g., earth normal modes, tides), which is the instruments main frequency band of interest. In the seismic band, above the resonant frequency, it is necessary to correct data for the instrument frequency response when comparing data with ground motion models. The recommendation of Francis et al. (2011) and others is emphasized, for operators to determine the full bandwidth frequency response of the instrument, similar to, for example, the Network Of Superconducting Gravimeters (1997), and publish the transfer function in widely used poles and zeros formats, for example, StationXML (Ahern et al., 2015).

For the purpose of quality assessment, the data are processed using a segment length of 1 h, therewith eliminating frequencies below 0.001 Hz. The low-frequency signals and spectral peaks (e.g., caused by earth tides) would be smoothed out regardless and contribute little value to quality control. The detection of changes in the seismic band is sufficient to confirm the instrument is performing as expected. The instrument in question (iGrav SG) clips at ± 10 V, with a sensitivity depending on configuration between 700 and 1,000 $\text{nm s}^{-2} \text{V}^{-1}$ below the resonant frequency, thus recording a maximum acceleration A of 7–10 $\mu\text{m s}^{-2}$. Internally, a 24-bit ADC digitizes the analog signal, placing the quantization noise far below the NLNM (Figure 14), also for frequencies below 0.001 Hz. The PPSD reaches the thermal noise floor due to Brownian

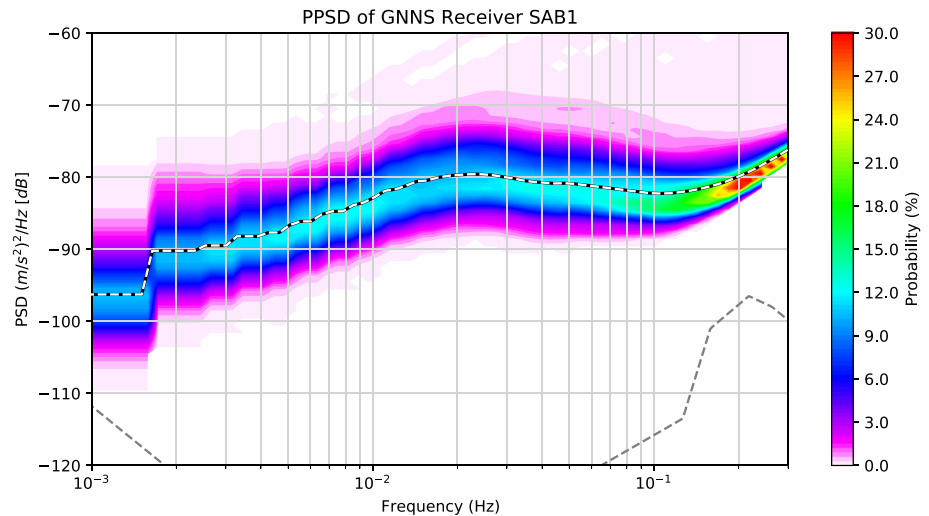


Figure 15. Showing the Probability density function (PPSD) of the vertical precise point position (PPP) displacement solutions (expressed in acceleration) of Global Navigation Satellite System (GNSS) station SAB1 from 2019, deployed on the volcanic island of Saba in the Caribbean Netherlands. The white dashed line is the median of the PPSD. The Peterson (1993) New High Noise Model (NHNM) is illustrated in gray.

motion in a mechanical oscillator at roughly -180 dB (Rosat & Hinderer, 2018; Warburton et al., 2010), further suggesting that no quantization noise is recorded at any frequency. When corrected for the instrument frequency response, the microseisms are clearly visible and can serve as another constraint on the PSD estimate for gravimeters.

3.2.8. GNSS Receivers

The ground displacement observations from GNSS receivers in the NSAN are utilized for the detection of volcanic deformation on the islands of Saba and St. Eustatius in the Caribbean Netherlands. Ground displacement data can be derived from high temporal resolution (>1 Hz) GNSS instruments that continuously record the position of the receiver against a reference earth ellipsoid. GNSS precise point position (PPP) solutions have inherently low precision, with a resolution on horizontal displacements between 2 and 4 mm and vertical displacements at the sub-centimeter level (Xu et al., 2013). Displacement solutions are often characterized by high-noise levels due to, for example, the variable number of satellites used for the inversion, environmental multipath reflections, and atmospheric variations. Despite the inherently low precision, GNSS data may contribute to the detection of large seismic events or rapidly occurring volcanic phenomena, such as caldera collapse (Elósegui et al., 2006; Neal et al., 2019; Wang et al., 2013). For the purpose of long-term volcano monitoring, the receiver position is conventionally averaged out to a single position per day with a higher precision. Raw GNSS data were processed using the PPP algorithm, using the open source RTKLIB package (Takasu, 2013) to find vertical displacement ground motion with a 1-Hz sampling rate. To express the ground displacement PSD in acceleration the estimate is multiplied by ω^2 to differentiate from displacement to acceleration in the frequency domain where the resulting PPSD is illustrated in Figure 15.

Because of the large scatter in observations, quantization noise is not expected to be visible in the PSD estimate and no theoretical noise model can be fitted following Equation 8. Furthermore, no global noise models exist and for lack of better alternatives, the only remaining yet most effective metric is the percentile criteria. Despite the proven contribution of this technique, automated GNSS anomaly detection is presently not included in the operational chain.

3.3. NSAN Instrument Quality Verification Procedure

In the following section, the quality control procedure and constraints that are applied to specific sets of instruments are discussed. The procedure is operated weekly on the latest monthly PPSD for each instrument. Not all instruments discussed in Section 3.2 are currently operational in the NSAN and this section

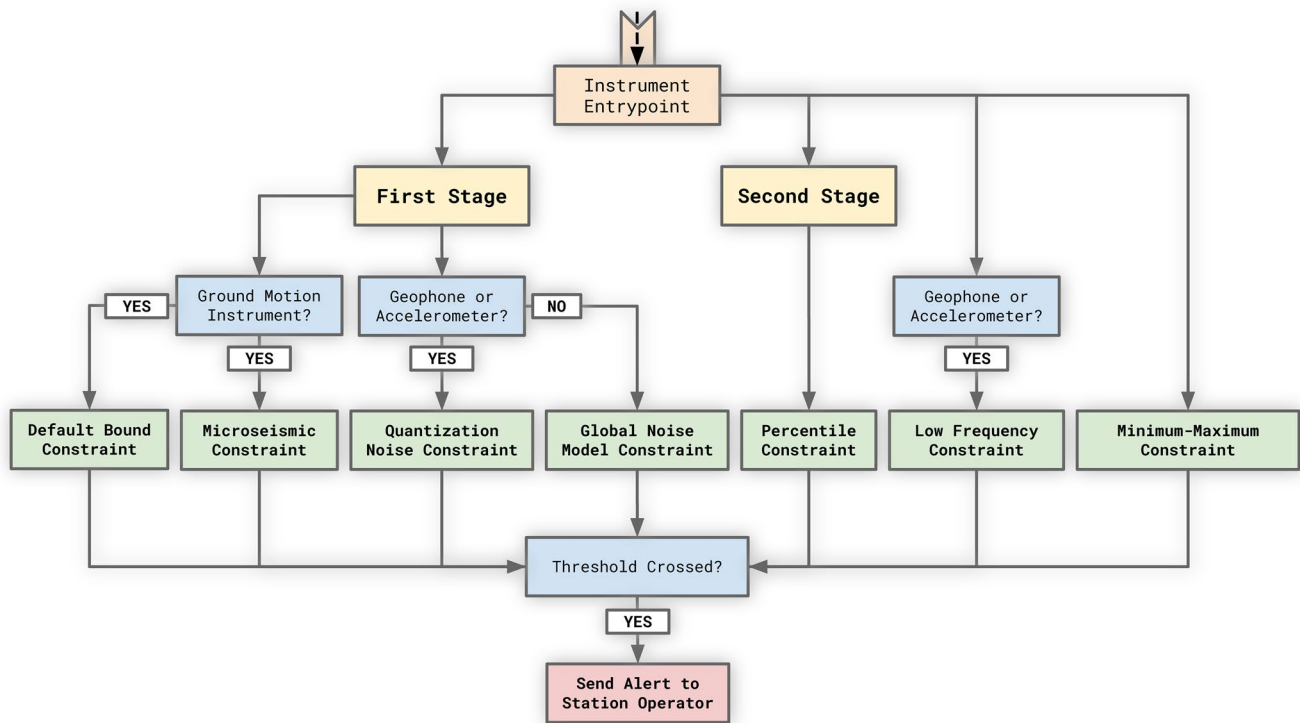


Figure 16. Schematic flowchart illustrating the probability density function (PPSD) quality assessment algorithm. The process is divided into two stages based on the availability of verified archived data and thus percentile confidence intervals. The algorithm can easily be extended for other types of data and the recommended quality criteria discussed in Sections 3.1 and 3.2.

is limited to the types of instruments that are. A flowchart of all the imposed constraints from Section 3.1 on the operational network is schematically visualized in Figure 16. This process can easily be extended for other types of instruments.

3.3.1. All Instruments

For all instruments it is confirmed there is a minimum scatter of 5 dB at ~3 Hz (Section 3.1.5). If the instrument is an accelerometer or geophone, the system verifies that the low-frequency constraint is passed (Section 3.1.4). The processing is then split into different paths for instruments in the different stages of quality control.

3.3.2. Instrument Stage Zero: New Installations

Instruments in the first month of operation are placed in this stage and do not contribute to operational workflows. This stage exists to evaluate the performance of an instrument in its environment before its data are used and published. This stage shares the metrics defined in stage one.

3.3.3. Instrument Stage One: Recent Installations

Instruments with less than one year of archived quality control passed data are kept in the first stage. Because archived data are absent for new stations the system falls back to comparison against generic limits following the flowchart illustrated in Figure 16. For stations in the first stage, the median of the PPSD of ground motion instruments is compared against the expected microseisms at 0.3 Hz (Section 3.1.3), and the default upper bound over all frequencies (Section 3.1.6). The theoretical quantization noise constraint described in Section 3.1.1 is applied for accelerometers and geophones where a theoretical lower bound of the instrumental noise is available. Instead, for broadband seismometers and infrasound stations the system compares the median against the instruments respective global noise model (Section 3.1.2). Instruments in stage one are promoted to stage two if more than a year of high-quality data has been archived.

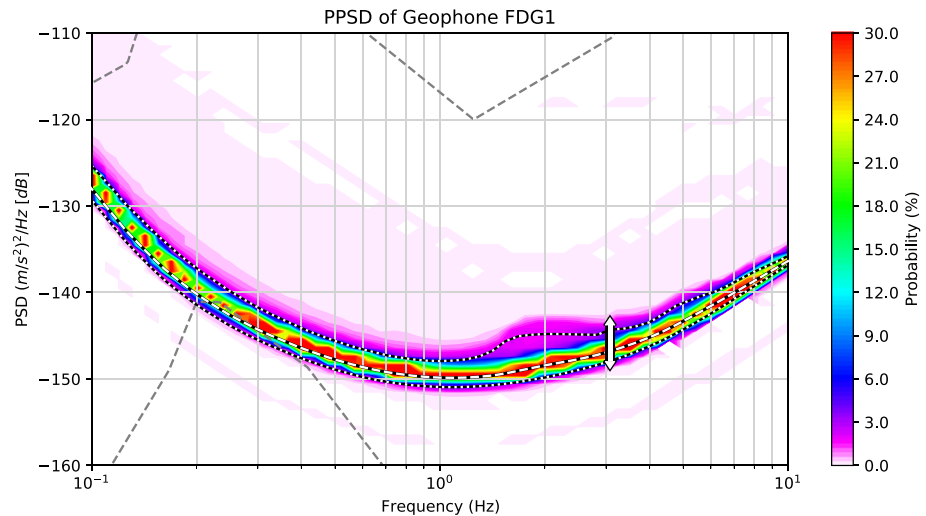


Figure 17. Showing geophone FDG1 (N-component) throughout 2019 that is dominated by instrumental noise over its full bandwidth. The range of the white arrow at ~ 3 Hz covers a 4-dB difference between the minimum and maximum that is insufficient to pass the minimum-maximum threshold of 5 dB (Section 3.1.5) and was raised for review by the system.

3.3.4. Instrumental Stage Two: Existing Installations

Stations in the second stage have their latest monthly median of power spectra compared against archived data that includes constraints on the local noise field around the instrument. The PPSD of validated archived data provides an upper and lower 2.5% confidence limit on the incoming data.

4. Results

4.1. Identification of Degraded Instrument Performance

In the following section three examples of degraded instrument performance are presented that were identified by the system in an operational setting.

4.1.1. Detection of Pure Instrumental Noise Recordings

Instruments with shorted inputs or dataloggers that are disconnected from the sensor only record intrinsic electrical noise. The PSD is expected to be stable and narrow over the full bandwidth. Geophone FDG1 shows an example of an instrument identified by the system that is recording only digitizer noise (Figure 17). This example fails the required minimum-maximum difference of 5 dB threshold discussed in Section 3.1.5.

4.1.2. High Noise at Low Frequencies

The PPSD of surface accelerometer BLOP illustrated in Figure 18 should be dominated by instrumental noise at lower frequencies. However, a clear scatter can be identified and the PPSD is nowhere near the expected quantization noise lower limit. Another undesirable process is introducing high levels of ambient noise and the cause should be investigated.

4.1.3. Percentile Threshold Trigger

Changes in the trend of the PSD estimates of an instrument can be detected by comparing statistical parameters of the latest PPSD against confidence percentiles calculated from previously archived spectra. The PPSD of station DR023 in Figure 19 shows the mean of the distribution of the latest month of data falling outside the expected percentile. This divergence of the ambient noise level was automatically detected and the station operator was notified. After this detection, the percentile constraint was changed to use the median of the PPSD instead of the mean.

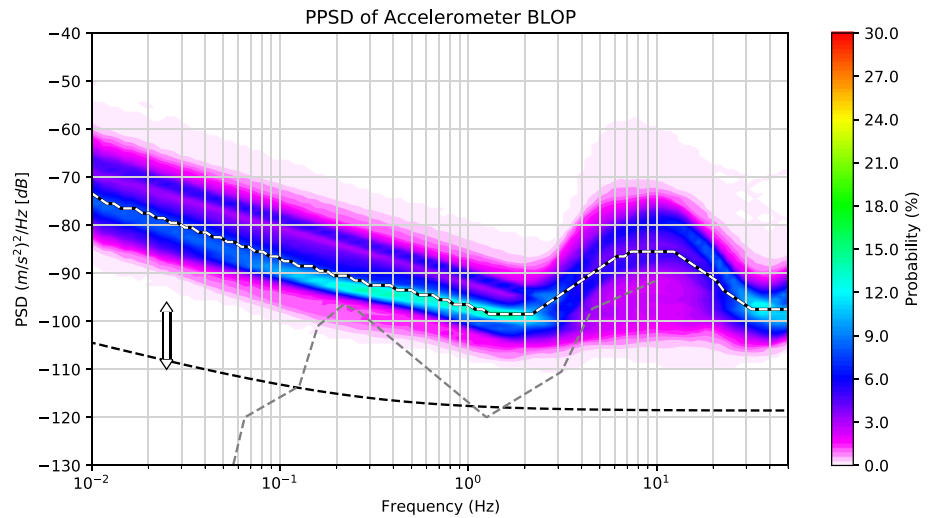


Figure 18. The median of the probability density function (PPSD; 2019) of surface accelerometer BLOP (vertical) does not fall within the required low-frequency threshold. The median of the distribution exceeds the theoretical model from Equation 8 (dashed black line) for a batch-1 accelerometer (Table 1) by more than 10 dB (white arrow) at 0.025 Hz and was therefore raised by the system.

5. Discussion

The amount of data flowing into the archive is growing rapidly and network operators must increasingly rely on automated and unsupervised processes to detect and identify instrumental anomalies. The main objective of the PSD database is to store spectral estimates as input for the automated quality control process for the NSAN. The spectral smoothing and binning makes the database less suitable for anomaly detection before the higher seismic frequency band (< 0.01 Hz), and for scientific purposes that require accurate resolution of spectral peaks (Anthony et al., 2020). Nonetheless, the system is designed as a data product for researchers and analysts that provides conventional PSD estimates for the entire NSAN archive without requiring any client-side resources for processing. The API is designed to aggregate and visualize PSD segments in various ways (e.g., PPSD, spectrogram, and power time series at a particular frequency) depending on the user preference. The presented database of individual PSD estimates is the most versatile and flexible

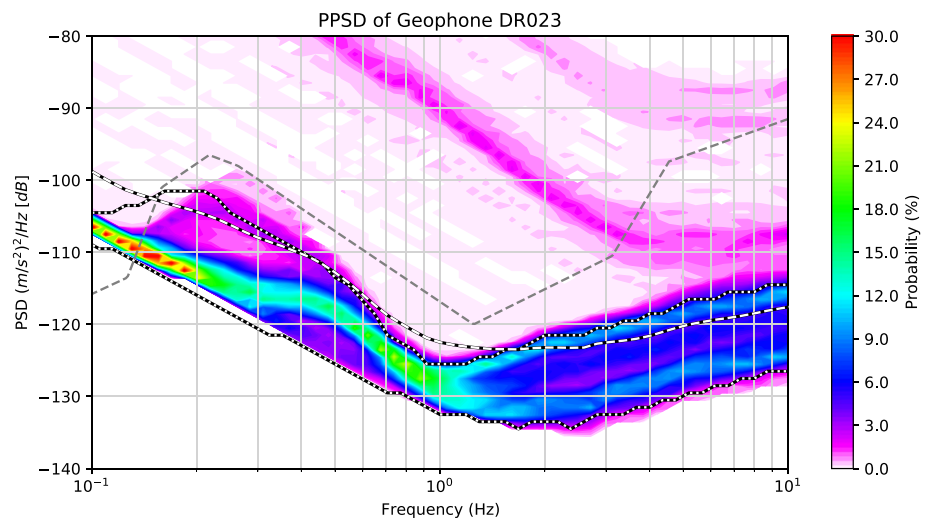


Figure 19. The mean of the probability density function (PPSD; dashed) of geophone DR023 (horizontal) during September 2020 exceeds the maximum (97.5th) archived percentiles (dotted) around 1 Hz, due to anomalously high power spectral density (PSD) estimates during the latest month. The percentiles were calculated from validated archived data.

way to cache spectral information. The fine granularity of the hourly segments makes the database valuable for studying transient signals present over a sufficiently large bandwidth, for example, looking at the footprint of anthropogenic noise (Lecocq et al., 2020), or developing and extending global noise models (Wolin & McNamara, 2019).

Because the PSD estimates are cached in the database, no processing is required except for the retrieval of the segments. One problem this approach introduces is that the instrument frequency response is already deconvolved from the data before it is stored. When the instrument transfer function is corrected by the operator, all cached PSD segments for this channel become invalid and need to be scheduled for reprocessing. Another option to consider is to store the PSD in counts and removing the instrument response during the request, adding some additional overhead but eliminating the need for reprocessing when metadata is altered.

Because the procedure is run weekly, using the past month of data, a delay in the detection is expected from the moment an instrument begins to perform poorly. The monthly median of the PPSD is used so that the PSD segments are averaged out for short-lived transient effects that may trigger the system as a false positive. An alternative consideration is to run the system at a daily interval. However, because of the slow evolution of the median of the PPSD, this will not significantly advance the moment of detection. Furthermore, with over 700 stations, having to review the results of the system trigger every day exceeds the available human resources at our disposal. Fine tuning of the system detection sensitivity is easily performed by changing configuration during the PSD calculation, for example, segment length, smoothing range, and fixed frequency interval. The sensitivity of the metrics can also be easily adjusted as well, by either raising or decreasing the thresholds for detection.

The presented database is highly efficient in terms of storage, amounting to only a total of less than 0.05% percent of the size of the NSAN data archive. In comparison, a database of uncompressed PSDs would occupy the same storage size as the waveform data does in the time domain. A significant reduction in size is introduced by the full-octave smoothing, fixed one-eighth frequency intervals, and rounding of power densities to the nearest dB to fit within a single-byte range. The presented custom compression scheme saves only a single 8-bit array per spectrum and the metadata required for the PSD reconstruction.

The number of proxybits η used to model the quantization noise of the datalogger are empirically derived from field data, using a part of frequency band that is dominated instrumental noise. The simple theoretical models are based on purely white quantization noise superimposed on a pink noise spectrum (f^{-1}) that works well for accelerometers, geophones, and tiltmeters that are dominated by instrumental noise. More accurate models for instrumentation self-noise could be found by conducting laboratory experiments through, for example, shorting of the datalogger input and measuring its output. The presented approach is based on simple theoretical models (Bennett, 1948; Sleeman, 2006) and empirical fitting because the NSAN employs many different types of instruments of varying generations that are currently operational in the field. This constraint will be able to detect a mismatch between the sensor output voltage and the datalogger input voltage (Table 1), or when a wrong instrument sensitivity is used. It should be emphasized that the system is unable to detect problems if the same error is made in computing PSD_{\min} and the instrument metadata, and suggest the model fitting is done independently from the metadata entry. Datalogger quantization noise models could not be empirically fitted for broadband seismometers, gravimeters, infrasonic stations, hydrophones and GNSS receivers. For these instruments, in the frequency band the system applies the automated quality control, environmental or sensor noise dominates over instrumental noise.

The derived confidence range of -90 to -140 dB for the microseisms is similar to the Peterson (1993) noise models at 0.3 Hz and may be partially redundant for the Netherlands. A more accurate model would include the relationship between coastal distances and the value of PSD estimate as illustrated in Figure 6, with a slope of approximately -0.15 dB km $^{-1}$. One downside of this change would be the detection of more false positives as the relationship is not fully consistent between all instrumental sites and does not include local site effects.

A number of different constraints for the detection of abnormal PSD estimates are applied, so that if one constraint fails to trigger as expected, the anomaly may be picked up by another independent metric that is based on a completely different characteristic of the PSD. In particular with the availability of confidence

intervals per station calculated on archived data that has been verified by the station operator, the system will be able to identify deviations from ordinary conditions within a week. The system is designed to support extensions with other types of instruments, for example, hydrophones, tiltmeters, gravimeters, and GNSS receivers that are presently not included in the NSAN, but may be in the future.

6. Conclusion

This study presents an operational implementation of a quality verification procedure for the NSAN is based on the automated analysis of PSD estimates. The system is designed to efficiently store PSD estimates in a database using a custom compression scheme. The NSAN is continuously expanding and interest in new and additional instrumentation is rapidly growing, thus highlighting the need for automated policies and procedures. A universal method is proposed to automatically verify the performance of many types of geophysical instruments in a technically similar way. The variation of PSD estimates through time from geophysical instruments serves as an effective mechanism to assess the performance of the instrument. The commonly used technique of using PSD estimates for quality control is applied and extended where additional quality criteria of the PSD are defined and recommended for different instruments. These criteria are based on (a) conventional global noise models, (b) instrument specific models based on digitizer quantization noise, (c) regional models for the Netherlands using the microseisms, and (d) site-local using data-driven statistical confidence limits. For the NSAN the automated procedure is scheduled weekly and verifies that the latest monthly archived waveform data falls within the limits imposed by our quality constraints defined in Section 3.1. This system proves promising for many geophysical instruments and can easily be adapted and extended in the future. It is shown that the system is able to monitor that instruments in the NSAN are operating as expected, and automatically detect degraded instrument performance at a national network scale.

Data Availability Statement

Data from the KNMI archive with Federation of Digital Seismograph Networks (FDSN) network identifiers NL (KNMI, 1993) and NA (KNMI, 2006) were used in the creation of this manuscript. The facilities of IRIS Data Services were used for access to waveforms and related metadata from the International Geodynamics and Earth Tide Service (Network Of Superconducting Gravimeters, 1997), the Clemson University Subsurface Deformation Monitoring Network (FDSN network code 2J; Scott DeWolf, 2016), and the International Miscellaneous Stations (FDSN network code IM) network. GNSS precise satellite orbit and clock solutions were downloaded from the Crustal Dynamics Data Information System (Noll, 2010). GPS data from the Caribbean Netherlands is attributed to De Zeeuw-van Dalen and Sleeman (2019). Figures were made with Matplotlib version 3.2.1 (Caswell et al., 2020; Hunter, 2007), available under the Matplotlib license at <https://matplotlib.org/>. Maps were created through PyGMT (prerelease) (Uieda et al., 2021) using Generic Mapping Tools (GMT) version 6 (Wessel et al., 2019a, 2019b) licensed under LGPL version 3 or later, available at <https://www.genericmapping-tools.org/>. Part of the software (version 1.0.0) associated with this manuscript for the calculation and storage of PSDs is licensed under MIT and published on GitHub <https://github.com/Jollyfant/psd-module/> (Jollyfant, 2021).

Acknowledgments

The authors thank the R&DSA software development team Jarek Bienkowski, Gert-Jan van den Hazel, and João Paulo Pereira Zanetti for their assistance in implementing the software stack. Jelle Assink provided his advice to process infrasound and hydroacoustic data. Elske de Zeeuw-Van Dalen provided the GNSS data and valuable support. Hans van der Marel is thanked for his advice in avoiding pitfalls encountered during GNSS PPP processing. Daniele Carbone and Michel Van Camp are thanked for sharing their experience with the iGrav superconducting gravimeters. The authors would like to thank the editor and three anonymous reviewers for their comments and suggestions that have helped us improve the final manuscript. The authors express our sincerest gratitude to the late Dr. Peter Fox.

References

- Ahern, T., Benson, R., Casey, R., Trabant, C., & Weertman, B. (2015). Improvements in data quality, integration and reliability: New developments at the IRIS DMC. *Advances in Geosciences*, 40, 31–35. <https://doi.org/10.5194/adgeo-40-31-2015>
- Ahern, T., Casey, R., Barnes, D., Benson, R., Knight, T., & Trabant, C. (2007). *Seed reference manual, version 2.4*. PLACE: Incorporated Research Institutions for Seismology.
- Anthony, R. E., Ringler, A. T., Wilson, D. C., Bahavar, M., & Koper, K. D. (2020). How processing methodologies can distort and bias power spectral density estimates of seismic background noise. *Seismological Research Letters*, 91(3), 1694–1706. <https://doi.org/10.1785/0220190212>
- Bennett, W. R. (1948). Spectra of quantized signals. *Bell System Technical Journal*, 27(3), 446–472. <https://doi.org/10.1002/j.1538-7305.1948.tb01340.x>
- Berger, J., Davis, P., & Ekström, G. (2004). Ambient earth noise: A survey of the global seismographic network. *Journal of Geophysical Research*, 109(B11). <https://doi.org/10.1029/2004jb003408>

- Beyreuther, M., Barsch, R., Krischer, L., Megies, T., Behr, Y., & Wassermann, J. (2010). ObsPy: A python toolbox for seismology. *Seismological Research Letters*, 81(3), 530–533. <https://doi.org/10.1785/gssrl.81.3.530>
- Brown, D., Ceranna, L., Prior, M., Mialle, P., & Bras, R. J. L. (2012). The IDC seismic, hydroacoustic and infrasound global low and high noise models. *Pure and Applied Geophysics*, 171(3–5), 361–375. <https://doi.org/10.1007/s00024-012-0573-6>
- Burtin, A., Bollinger, L., Vergne, J., Cattin, R., & Nábělek, J. (2008). Spectral analysis of seismic noise induced by rivers: A new tool to monitor spatiotemporal changes in stream hydrodynamics. *Journal of Geophysical Research*, 113(B5). <https://doi.org/10.1029/2007jb005034>
- Camelbeeck, T., & van Eck, T. (1994). The roer valley graben earthquake of 13 April 1992 and its seismotectonic setting. *Terra Nova*, 6(3), 291–300. <https://doi.org/10.1111/j.1365-3121.1994.tb00499.x>
- Carbone, D., Antoni-Micollier, L., Hammond, G., Zeeuw-van Dalfsen, D., Rivalta, E., Bonadonna, C., et al. (2020). The newton-g gravity imager: Towards new paradigms for terrain gravimetry. *Frontiers of Earth Science*, 8, 452. <https://doi.org/10.3389/feart.2020.573396>
- Carbone, D., & Greco, F. (2007). Review of microgravity observations at Mt. Etna: A powerful tool to monitor and study active volcanoes. *Pure and Applied Geophysics*, 164(4), 769–790. <https://doi.org/10.1007/s00024-007-0194-7>
- Castellaro, S., & Mulargia, F. (2012). A statistical low noise model of the earth. *Seismological Research Letters*, 83(1), 39–48. <https://doi.org/10.1785/gssrl.83.1.39>
- Caswell, T., Droettboom, M., Lee, A., Hunter, J., Firing, E., Stansby, D., et al. (2020). Matplotlib v3.2.1 [Software]. Zenodo. <https://doi.org/10.5281/zenodo.3714460>
- Cauzzi, C., & Clinton, J. (2013). A high- and low-noise model for high-quality strong-motion accelerometer stations. *Earthquake Spectra*, 29(1), 85–102. <https://doi.org/10.1193/1.4000107>
- Cooley, J. W., & Tukey, J. W. (1965). An algorithm for the machine calculation of complex Fourier series. *Mathematics of Computation*, 19(90), 297–301. <https://doi.org/10.1090/s0025-5718-1965-0178586-1>
- Coyne, J., Bobrov, D., Bormann, P., Duran, E., Grenard, P., Haralabus, G., & Starovoi, Y. (2012). Ctbto: Goals, networks, data analysis and data availability. In *New Manual of Seismological Observatory Practice 2 (NMSOP-2)* (pp. 1–41). Deutsches GeoForschungsZentrum GFZ.
- De Zeeuw-van Dalfsen, E., & Sleeman, R. (2018). A permanent, real-time monitoring network for the volcanoes mount scenery and the quill in the Caribbean Netherlands. *Geosciences*, 8(9), 320. <https://doi.org/10.3390/geosciences8090320>
- De Zeeuw-van Dalfsen, E., & Sleeman, R. (2019). KNMI Dutch Antilles GPS Network [Dataset]. UNAVCO, Inc. <https://doi.org/10.7283/633E-1497>
- Dost, B. (1994). The orfeus data center. *Annals of Geophysics*, 37(5). <https://doi.org/10.4401/ag-4198>
- Dost, B., & Haak, H. (2002). *A comprehensive description of the KNMI seismological instrumentation*. Royal Netherlands Meteorological Institute.
- Dzurisin, D. (2003). A comprehensive approach to monitoring volcano deformation as a window on the eruption cycle. *Reviews of Geophysics*, 41(1). <https://doi.org/10.1029/2001rg000107>
- Elósegui, P., Davis, J., Oberlander, D., Baena, R., & Ekström, G. (2006). Accuracy of high-rate GPS for seismology. *Geophysical Research Letters*, 33(11). <https://doi.org/10.1029/2006gl026065>
- Evers, L. G., Ceranna, L., Haak, H. W., Le Pichon, A., & Whitaker, R. W. (2007). A seismoacoustic analysis of the gas-pipeline explosion near Ghislenghien in Belgium. *Bulletin of the Seismological Society of America*, 97(2), 417–425. <https://doi.org/10.1785/0120060061>
- Francis, O., Lampitelli, C., Klein, G., Van Camp, M., & Palinkas, V. (2011). Comparison between the transfer functions of three superconducting gravimeters. *Marees Terrestres: Bulletin d'Informations*, 147, 11857–11868.
- García, A., Ortiz, R., Marrero, J. M., Sánchez, N., Vila, J., Correig, A. M., et al. (2006). Monitoring the reawakening of Canary Islands' Teide volcano. *Eos, Transactions American Geophysical Union*, 87(6), 61–65. <https://doi.org/10.1029/2006eo060001>
- Havskov, J., & Alguacil, G. (2016). *Instrumentation in earthquake seismology*. Springer International Publishing. <https://doi.org/10.1007/978-3-319-21314-9>
- Heinzel, G., Rüdiger, A., & Schilling, R. (2002). *Spectrum and spectral density estimation by the Discrete Fourier Transform (DFT), including a comprehensive list of window functions and some new flat-top windows* (Vol. 12). Max Plank Institute.
- Hunter, J. D. (2007). Matplotlib: A 2d graphics environment. *Computing in Science & Engineering*, 9(3), 90–95. <https://doi.org/10.1109/MCSE.2007.55>
- Jollyfant. (2021). Jollyfant/psd-module: Version 1.0.0 [Software]. Zenodo. <https://doi.org/10.5281/zenodo.4964159>
- Kimman, W., Campman, X., & Trampert, J. (2012). Characteristics of seismic noise: Fundamental and higher mode energy observed in the northeast of the Netherlands. *Bulletin of the Seismological Society of America*, 102(4), 1388–1399. <https://doi.org/10.1785/0120110069>
- KNMI. (1993). Netherlands seismic and acoustic network [Dataset]. Royal Netherlands Meteorological Institute (KNMI). <https://doi.org/10.21944/e970fd34-23b9-3411-b366-e4f72877d2c5>
- KNMI. (2006). Caribbean Netherlands seismic network [Dataset]. Royal Netherlands Meteorological Institute (KNMI), Other/Seismic Network. <https://doi.org/10.21944/dfa7a3f-7e3a-3b33-a436-516a01b6af3f>
- Lecocq, T., Hicks, S. P., Noten, K. V., van Wijk, K., Koelemeijer, P., Plaen, R. S. M. D., et al. (2020). Global quieting of high-frequency seismic noise due to COVID-19 pandemic lockdown measures. *Science*, 369(6509), 1338–1343. <https://doi.org/10.1126/science.abd2438>
- McNamara, D. E., & Boaz, R. (2006a). Pqlx: A software tool to evaluate seismic station performance. In *AGU Fall Meeting Abstracts*.
- McNamara, D. E., & Boaz, R. (2006b). Seismic noise analysis system using power spectral density probability density functions: A stand-alone software package. *Citeseer*.
- McNamara, D. E., & Buland, R. P. (2004). Ambient noise levels in the continental United States. *Bulletin of the Seismological Society of America*, 94(4), 1517–1527. <https://doi.org/10.1785/012003001>
- McNamara, D. E., Hutt, C., Gee, L., Benz, H. M., & Buland, R. (2009). A method to establish seismic noise baselines for automated station assessment. *Seismological Research Letters*, 80(4), 628–637. <https://doi.org/10.1785/gssrl.80.4.628>
- Ménoret, V., Vermeulen, P., Le Moigne, N., Bonvalot, S., Bouyer, P., Landragin, A., & Desruelle, B. (2018). Gravity measurements below 10⁻⁹ g with a transportable absolute quantum gravimeter. *Scientific Reports*, 8(1), 1–11. <https://doi.org/10.1038/s41598-018-30608-1>
- Mentink, J. H., & Evers, L. G. (2011). Frequency response and design parameters for differential microbarometers. *Journal of the Acoustical Society of America*, 130(1), 33–41. <https://doi.org/10.1121/1.3596718>
- Middlemiss, R., Samarelli, A., Paul, D., Hough, J., Rowan, S., & Hammond, G. (2016). Measurement of the earth tides with a mems gravimeter. *Nature*, 531(7596), 614–617. <https://doi.org/10.1038/nature17397>
- Neal, C. A., Brantley, S., Antolik, L., Babb, J., Burgess, M., Calles, K., et al. (2019). The 2018 rift eruption and summit collapse of Kilauea volcano. *Science*, 363(6425), 367–374. <https://doi.org/10.1126/science.aav7046>
- Network of Superconducting Gravimeters. (1997). International geodynamics and earth tide service [Dataset]. International Federation of Digital Seismograph Networks. <https://doi.org/10.7914/SN/SG>

- Noll, C. E. (2010). The crustal dynamics data information system: A resource to support scientific analysis using space geodesy. *Advances in Space Research*, 45(12), 1421–1440. <https://doi.org/10.1016/j.asr.2010.01.018>
- Oppenheim, A. V., & Schaffer, R. W. (2009). *Discrete-time signal processing* (3rd ed.). Prentice Hall Press.
- Pedersen, H. A., Leroy, N., Zigone, D., Vallée, M., Ringler, A. T., & Wilson, D. C. (2020). Using component ratios to detect metadata and instrument problems of seismic stations: Examples from 18 yr of geoscope data. *Seismological Research Letters*, 91(1), 272–286. <https://doi.org/10.1785/0220190180>
- Petersen, G. M., Cesca, S., & Kriegerowski, M., & AlpArray Working Group. (2019). Automated quality control for large seismic networks: Implementation and application to the AlpArray seismic network. *Seismological Research Letters*, 90(3), 1177–1190. <https://doi.org/10.1785/0220180342>
- Peterson, J. R. (1993). Observations and modeling of seismic background noise. *US Geological Survey*. <https://doi.org/10.3133/ofr93322>
- Ringler, A. T., Hagerty, M., Holland, J., Gonzales, A., Gee, L. S., Edwards, J., et al. (2015). The data quality analyzer: A quality control program for seismic data. *Computers & Geosciences*, 76, 96–111. <https://doi.org/10.1016/j.cageo.2014.12.006>
- Rosat, S., & Hinderer, J. (2018). Limits of detection of gravimetric signals on earth. *Scientific Reports*, 8(1), 1–8. <https://doi.org/10.1038/s41598-018-33717-z>
- Rosat, S., Hinderer, J., Crossley, D., & Boy, J. (2004). Performance of superconducting gravimeters from long-period seismology to tides. *Journal of Geodynamics*, 38(3–5), 461–476. <https://doi.org/10.1016/j.jog.2004.07.005>
- Ruigrok, E., Domingo-Ballesta, J., van den Hazel, G.-J., Dost, B., & Evers, L. (2019). Groningen explosion database. *First Break*, 37(8), 37–41. <https://doi.org/10.3997/1365-2397.n0053>
- Scott DeWolf, L. C. M. (2016). Clemson university subsurface deformation monitoring network [Dataset]. International Federation of Digital Seismograph Networks. https://doi.org/10.7914/SN/2J_2016
- Sleeman, R. (2006). Three-channel correlation analysis: A new technique to measure instrumental noise of digitizers and seismic sensors. *Bulletin of the Seismological Society of America*, 96(1), 258–271. <https://doi.org/10.1785/0120050032>
- Sleeman, R., Haak, H., Bos, M., & Van Gend, J. (2000). Tidal tilt observations in the Netherlands using shallow borehole tiltmeters. *Physics and Chemistry of the Earth – Part A: Solid Earth and Geodesy*, 25(4), 415–420. [https://doi.org/10.1016/s1464-1895\(00\)00065-x](https://doi.org/10.1016/s1464-1895(00)00065-x)
- Sparks, R., Biggs, J., & Neuberg, J. (2012). Monitoring volcanoes. *Science*, 335(6074), 1310–1311. <https://doi.org/10.1126/science.1219485>
- Spetzler, J., & Dost, B. (2017). Hypocentre estimation of induced earthquakes in Groningen. *Geophysical Journal International*, 209(1), 453–465.
- Steim, J. (2015). *Theory and observations-instrumentation for global and regional seismology*.
- Stonebraker, M., Brown, P., Zhang, D., & Becla, J. (2013). SciDB: A database management system for applications with complex analytics. *Computing in Science & Engineering*, 15(3), 54–62. <https://doi.org/10.1109/mcse.2013.19>
- Strollo, A., Evans, P., Heinloo, A., Hemmleb, S., Hillmann, L., Jäckel, K.-H., et al. (2020). *Geofon annual report 2019*.
- Sugihara, M., & Ishido, T. (2008). Geothermal reservoir monitoring with a combination of absolute and relative gravimetry. *Geophysics*, 73(6), WA37–WA47. <https://doi.org/10.1190/1.2991105>
- Takasu, T. (2013). Rtklib ver. 2.4. 2 manual. In *RTKLIB: An Open Source Program Package for GNSS Positioning* (pp. 29–49).
- Trani, L., Koymans, M., Atkinson, M., Sleeman, R., & Filgueira, R. (2017). Wfcatalog: A catalogue for seismological waveform data. *Computers & Geosciences*, 106, 101–108. <https://doi.org/10.1016/j.cageo.2017.06.008>
- Uieda, L., Tian, D., Leong, W. J., Toney, L., Schlitzer, W., Yao, J., et al. (2021). PyGMT: A Python interface for the generic mapping tools [Software]. Zenodo. <https://doi.org/10.5281/zenodo.4592991>
- Van Camp, M., de Viron, O., Watlet, A., Meurers, B., Francis, O., & Caudron, C. (2017). Geophysics from terrestrial time-variable gravity measurements. *Reviews of Geophysics*, 55(4), 938–992. <https://doi.org/10.1002/2017rg000566>
- Van Der Walt, S., Colbert, S. C., & Varoquaux, G. (2011). The NumPy array: A structure for efficient numerical computation. *Computing in Science & Engineering*, 13(2), 22–30. <https://doi.org/10.1109/mcse.2011.37>
- Wang, R., Parolai, S., Ge, M., Jin, M., Walter, T. R., & Zschau, J. (2013). The 2011 Mw 9.0 Tohoku earthquake: Comparison of GPS and strong-motion data. *Bulletin of the Seismological Society of America*, 103(2B), 1336–1347. <https://doi.org/10.1785/0120110264>
- Warburton, R., Pillai, H., & Reineman, R. (2010). Initial results with the new GWR IGRAV superconducting gravity meter. In *Extended Abstract Presented at 2nd Asia Workshop on Superconducting Gravimetry Taipei, Taiwan*.
- Welch, P. (1967). The use of Fast Fourier Transform for the estimation of power spectra: A method based on time averaging over short, modified periodograms. *IEEE Transactions on Audio and Electroacoustics*, 15(2), 70–73. <https://doi.org/10.1109/tau.1967.1161901>
- Wessel, P., Luis, J. F., Uieda, L., Scharroo, R., Wobbe, F., Smith, W. H. F., & Tian, D. (2019a). The generic mapping tools version 6 [Software]. Zenodo. (Funded by US National Science Foundation grants OCE-1558403 and EAR-1829371). <https://doi.org/10.5281/zenodo.3407866>
- Wessel, P., Luis, J. F., Uieda, L., Scharroo, R., Wobbe, F., Smith, W. H. F., & Tian, D. (2019b). The generic mapping tools version 6. *Geochemistry, Geophysics, Geosystems*, 20(11), 5556–5564. <https://doi.org/10.1029/2019gc0008515>
- Wolin, E., & McNamara, D. E. (2019). Establishing high-frequency noise baselines to 100 Hz based on millions of power spectra from IRIS MUSTANG. *Bulletin of the Seismological Society of America*, 110(1), 270–278. <https://doi.org/10.1785/0120190123>
- Xu, P., Shi, C., Fang, R., Liu, J., Niu, X., Zhang, Q., & Yanagidani, T. (2013). High-rate precise point positioning (PPP) to measure seismic wave motions: An experimental comparison of GPS ppp with inertial measurement units. *Journal of Geodesy*, 87(4), 361–372. <https://doi.org/10.1007/s00190-012-0606-z>